

STATE RESEARCH CENTER OF RUSSIA
INSTITUTE FOR HIGH ENERGY PHYSICS

Conceptual Design
of the Narrow Band Beam Absorber
and Low Energy Wide Band Beam Calculations
for the NuMI Project

(Task B Report of the Accord between FNAL and IHEP)

A.Abramov, I.Azhgirey, P.Galkin, N.Galyaev, V.Garkusha,
A.Kharlamov, I.Kurochkin, E.Lomakin, F.Novoskoltsev,
A.Ryabov, V.Zapolsky, V.Zarucheisky

Protvino 1998

Contents

1	Beam Absorber for the Narrow Band Beam	3
1.1	General Description of the Beam Absorber	3
1.2	Incident Energy Characteristics in front of the Absorber . .	5
1.3	Energy Deposition in the Absorber Corebox	6
1.4	Cooling System of the Absorber	8
1.5	Temperature and Stress Analysis	9
1.5.1	Temperature calculations	9
1.5.2	Stress analysis	9
1.5.3	Emergency in the corebox of the absorber	10
1.6	Summary	11
2	Low Energy Wide Band Beam	29
2.1	Focusing Systems	29
2.2	Neutrino Event Rates at the Far Detector	31
2.3	Depth of Focus	33
2.4	Decay Region	34
2.5	Higher Energy Performance	34
2.6	Target	35
2.7	Summary	36

1 Beam Absorber for the Narrow Band Beam

The NBB absorber considered in this Section is significantly changed in comparison with its preliminary design [1]. The absorber corebox was moved 30 cm upstream the proton beam and the NBN magnet was shifted 60 cm downstream the beam in order to put additional iron shielding 1.4 m long between the corebox and NBN magnet. The corebox was surrounded by an iron with beam collimator inside. This iron together with iron shielding placed behind the aluminum section of the absorber should prevent the irradiation of the NBN magnet coils.

1.1 General Description of the Beam Absorber

The location of the beam absorber in the narrow band beam line is shown in Figure 1.1, its longitudinal cross-section and frontal view are given in Figure 1.2. The graphite part of the absorber corebox consists of eight 25 cm long and 160 mm in diameter cylinders of fine grain carbon (see Figure 1.3a). The total length of the graphite part is equal to 2.0 m ($\sim 4\lambda_C$). The diameter of a graphite core is determined by the possible positions of the proton beam for different NBB tunes, as well as by the neutral direction from the target.

The graphite core is held in 3.0 m long water-cooled aluminum jacket with 160 mm diameter hole bored 2.0 m deep along its axis. The length of aluminum along the absorber axis is equal to 1.0 m ($\sim 2.6\lambda_{Al}$). The transversal size of aluminum jacket is limited by the vertical beam aperture and is equal to 230 mm. A light shrinkfit of 0.06 mm is necessary to insure good thermal contact between the graphite cylinders and the aluminum jacket. Such shrinkfit corresponds to the maximum compressive strength in a graphite of 4.0 MPa. The shrinkfit should be not lost after the beam heating of corebox. The corebox housing should be made of a weldable, machinable, moderate strength aluminum alloy having good corrosion resistance.

In order to prevent oxidation of the graphite, a 0.15 mm thick titanium window seals and separates the graphite cylinders in dry nitrogen environment. The temperature of the graphite cylinders and the aluminum housing should be monitored using the thermocouples or resistive thermometers.

The graphite and aluminum are chosen the same as in the beam absorber corebox for the FNAL Main Injector Abort System [3],[4]. An overall reliability of these materials in high radioactive environment is confirmed by its successful operation for a long time. The properties of these materials are listed in Table 1.1 and Table 1.2 respectively.

Compressive Strength	90.0 MPa
Modulus of Elasticity	$11.0 \cdot 10^3$ MPa
Poisson Ratio	0.2
Thermal Conductivity	100 W/m/K
Coefficient of Thermal Expansion	$2.9 \cdot 10^{-6}$ 1/K
Specific Heat	709 J/kg/K
Density	1.73 g/cm^3
Melting Point	2600°C
Porosity	15%
Pore size	2.1 mm

Table 1.1: Room temperature properties of SGL Carbon Grade 7340.

Yield Strength	193.0 MPa
Tensile Strength	303 MPa
Fatigue Strength ($5 \cdot 10^8$ cycles)	158.6 MPa
Modulus of Elasticity	$70.8 \cdot 10^3$ MPa
Poisson Ratio	0.33
Elongation	16%
Thermal Conductivity	177.0 W/m/K
Coefficient of Thermal Expansion	$22.5 \cdot 10^{-6}$ 1/K
Specific Heat	875.0 J/kg/K
Density	2.77 g/cm^3
Melting Point	574°C

Table 1.2: Room temperature properties of 5083–H112 Aluminum Alloy.

The iron section of the absorber is divided into two parts:

- movable part which is fixed by means of two filler modules (see Figure 1.4). These filler modules should provide an alignment of the movable part of the absorber with respect to the beam. The transversal sizes of this part of the absorber are equal to $70 \times 70 \text{ cm}^2$ and the total weight of the whole assembly does not exceed 20 000 kg. The general view of the movable part of the beam absorber with NBB collimator is shown in Figure 1.3b.
- unmovable part, which is not shown in Figure 1.4, may be mounted from the steel blocks planned to be used for the upper steel shielding of the beam line.

All water and dry nitrogen pipes, electrical cables pass through the holes in the filler modules.

1.2 Incident Energy Characteristics in front of the Absorber

The investigation of particle distributions in front of the absorber, as well as calculation of the energy deposition in the absorber, has been carried out using the Monte Carlo computer code MARS'96 [2]. This program simulates the three dimensional hadron and electromagnetic cascades, taking into account the real geometry of narrow band beam line. The general view of narrow band beam line is shown in Figure 1.1. The NBB graphite target with 4 mm in diameter has the length of 50 cm ($\sim \lambda_C$). Focusing device FD1 is an assembly of two bolted together parabolic lenses with feeding current of 320 kA. The real field map in the NBR magnets is computed by program POISSON and is taken into account in beam simulations as well as the magnetic field in FD1 and particle interaction with its material.

The incident energy density distribution at the face of the absorber for the 45 GeV/c NBB tune per one primary proton is practically the same as one shown in the preliminary design Report (see Figure 1.3 of [1]). The incident energy distribution for the 20 GeV/c NBB tune is similar to the mentioned above with the exception of the proton peak position which is located approximately at the center of the absorber corebox. The energy of the incident beam in front of the absorber and corebox per one primary proton for both NBB tunes are given in Table 1.3.

The data of this Table show that the total incident energy in front of the absorber as well as of the corebox for 20 GeV/c tune is greater than

for 45 GeV/c one. It may be explained by lower beam dispersion in the magnets NBR for 20 GeV/c tune and is confirmed by the equality of neutral component (neutrons and gammas) of the energy.

Front cross-section, cm ²	100×100		23×23	
NBB tune, GeV/c	20	45	20	45
Total energy in a beam	71.67	70.00	64.69	61.71
Proton energy	60.96	60.42	58.86	57.01
Neutron energy	3.43	3.41	2.81	2.80
Pion energy	5.22	4.28	1.96	0.90
Gamma energy	1.59	1.60	0.97	0.98
Electron energy	0.47	0.29	0.10	0.02

Table 1.3: The incident energy (in GeV) in front of the absorber (100×100 cm²) and absorber corebox (23×23 cm²).

The hardest situation for the beam absorber arises when the target is out of primary proton beam. In this case a few spills of primary proton beam with the parameters given in Table 1.4 should be absorbed without destruction of the beam absorber.

Beam energy	120 GeV
Total kinetic energy	0.768 MJ
Pulse duration	1.0 ms
Short term continuous operation	1 or 2 spills
Number of protons per spill	$4 \cdot 10^{13}$
Transverse beam size (Gaussian beam distribution), $\sigma_x \times \sigma_y$	1.0×1.2 mm ²

Table 1.4: Primary proton beam parameters in front of the absorber corebox with the target out of the beam.

1.3 Energy Deposition in the Absorber Corebox

The energy deposition was calculated on a per grid zone basis. The transversal zone size varies from 0.2 cm near the beam axis to 1.0 cm at the outer perimeter. Along the azimuthal axis, Δz is alternated with 3 cm

and 30 cm. In case when the target is out of beam, the transversal zone size in the beam axis region was reduced to 0.05 cm in accordance with the proton beam size.

The distribution of deposited energy per one primary proton in the core-box of the absorber as a function of longitudinal coordinate z for both tunes and for the case when the target is out of beam are given in Figure 1.5. The distribution of dE/dz has three peaks: at $z = 165$ cm (graphite section), at $z = 233$ cm (aluminum section) and at $z = 320$ cm (iron section). Dashed line corresponds to the 20 GeV/c tune and lies slightly higher than solid line (45 GeV/c tune) that corresponds to the incident energy distribution in front of the corebox. Dotted line gives dE/dz for the hardest situation in the case of 45 GeV/c tune, when the target is out of proton beam. The longitudinal distribution of the maximum energy deposition density (ϵ) for this case is shown in Figure 1.6. The first peak arises in the graphite section and has the value of $7 \cdot 10^{-2}$ GeV/cm³, which is an order of magnitude greater than the same peak for the normal operation condition (see Figure 1.4 of [1]). The second peak corresponds to the aluminum section and is equal to $\sim 1.2 \cdot 10^{-2}$ GeV/cm³, that is ~ 5.5 times greater than that for the normal operation condition.

The results of the MARS'96 simulations of the power deposition in the absorber are summarized in Table 1.5. The investigation of transversal distribution of absorbed power in the iron surrounding the corebox shows that more than 90% of the power is deposited in the square with the sizes of 70×70 cm². It corresponds to the maximum weight of absorber less than 20 000 kg.

NBB tune, GeV/c	20	45
Total deposited power in the absorber	210.2	204.2
Deposited power in the corebox	112.5	105.9
Absorbed power in the iron shielding around the corebox	84.6	86.0
Absorbed power in the iron shielding behind the corebox	13.0	12.3

Table 1.5: Average power (in kW) deposited in the beam absorber at the beam intensity of $4 \cdot 10^{13}$ protons/spill with repetition period of 1.9 s.

The results of the absorbed doses calculations in the NBN magnet coils are given in Table 1.6. As follows from this Table, the absorbed dose has the maximum value of $6.7 \cdot 10^6$ Gy/year in the external windings close to the beam collimator and a usual reinforced organic insulation may be used for the coil fabrication in a case of three years operation period.

Tune	External winding			Internal winding	
	center	upper	down	upper	down
20 GeV/c	$4.45 \cdot 10^6$	$2.25 \cdot 10^6$	$5.52 \cdot 10^5$	$1.10 \cdot 10^6$	$4.32 \cdot 10^5$
45 GeV/c	$6.71 \cdot 10^6$	$2.38 \cdot 10^6$	$1.02 \cdot 10^6$	$1.21 \cdot 10^6$	$7.09 \cdot 10^5$

Table 1.6: Absorbed doses (in Gy/year) in the NBN magnet coils for $3.7 \cdot 10^{20}$ protons/year.

1.4 Cooling System of the Absorber

The corebox absorbs approximately 106 kW (average power) of the beam total energy for 45 GeV/c tune and 112.5 kW for 20 GeV/c tune, with remainder deposited in the iron shielding of the absorber (97.6 kW and 98.3 kW for 45 GeV/c and 20 GeV/c tunes respectively). The cooling system of the corebox has 8 water channels with a total flow rate of 106.4 l/min (28 gpm) in four parallel paths through the aluminum section of the corebox. Contrary to the preliminary design, the cooling channels are rotated at the angle of 22.5° with respect to the symmetric planes of the corebox. It allows to reinforce the weaker part of aluminum section. The diameter of each water channel is equal to 12.7 mm (1/2") and the water velocity is chosen 3.5 m/s which corresponds to the heat transfer coefficient of 12 kW/m²/K. The pressure drop is equal to 1.345 atm (19.2 psi) with ΔT of the water at (28.5–30)°C depending on a NBB tune.

The analysis of thermal steady state of the iron shielding under natural convection taking into account the air properties dependence on the temperature gives for the iron surface temperature the value of $\sim 320^\circ\text{C}$. It may cause an additional thermal load to the NBN coils as well as to the corebox cooling system. For this reason it is expedient to have a separate water cooling system of the iron shielding with a total water flow rate ~ 50 l/min. This cooling system may be made from stainless steel tubes welded at the external surface of the iron shielding.

1.5 Temperature and Stress Analysis

The temperatures and stresses in the absorber corebox have been computed by finite element program HAST [5], using the energy deposition distributions obtained from MARS'96 simulations. The origin of coordinate system for the temperature and stress calculations corresponds to the corebox axis with X-axis having direction to the right and Y-axis upward.

1.5.1 Temperature calculations

In order to obtain the temperature distributions in the corebox, the three dimensional nonstationary thermal problem has been simulated taking into account the variation of material properties with temperature and the cooling system described above. The heating of cooling water has been not considered.

As for the preliminary design of the absorber corebox [1] the steady states in graphite and aluminum are reached in about 100–150 pulses. The results of the calculations at steady state after a beam pulse are given in the form of two dimensional temperature distributions for both 20 GeV/c and 45 GeV/c tunes in Figures 1.7 and 1.8, respectively. The maximum temperatures arise along the axis of non-interacted with the target proton beam and are shown as the functions of azimuthal coordinate in Figure 1.9. For the 20 GeV/c tune the maximum temperature T_{\max} in the graphite section before a pulse is equal to 84°C at the point with coordinates: $y=-0.67$ cm and $z=140$ cm, whereas after the beam pulse the point of the maximum temperature is shifted to $y=-0.45$ cm and $z=120$ cm and T_{\max} has the value of 104°C. Similar values for the 45 GeV/c tunes are equal: before pulse $T_{\max}=77^\circ\text{C}$ at $y=3.93$ cm and $z=120$ cm, after pulse $T_{\max}=97^\circ\text{C}$ at $y=4.71$ cm and $z=100$ cm. The maximum temperature jump corresponds to the maximum density of deposited energy along the beam axis ($z=40$ cm) and is equal to 32.6°C for 20 GeV/c tune and 34.5°C for 45 GeV/c tune.

1.5.2 Stress analysis

Since the temperature gradient in Z-direction is rather small, the stress calculations have been made in two dimensional approach at the points corresponding to the maximum density of deposited energy along the beam axis and to the maximum temperature in the materials, taking into account

the preloading caused by a light shrinkfit (0.06 mm). The friction coefficient between graphite and aluminum is taken as zero, i.e. the graphite may slip fluently on the aluminum.

The resultant stresses (thermal & preloading) in the cross sections corresponding to the maximum density of deposited energy at the beam axis and to the maximum energy deposition in graphite and aluminum sections for the 20 GeV/c tune are shown in Figures 1.10–1.12. Similar plots for 45 GeV/c tune are given in Figures 1.13–1.15. As follows from these plots, the S_{rr} stress in the graphite is always negative, i.e. it is compressed and good thermal contact between graphite and aluminum is not lost due to the beam heating. The shape of stresses along the contact line between graphite and aluminum reflects well the structure of the cooling system.

The maximum equivalent stress (S_{eq}) is reached in aluminum section and is equal to 39.5 MPa for 20 GeV/c tune (point: $x=3.78$ cm, $y=-10.15$ cm and $z=220$ cm) and 39.7 MPa for 45 GeV/c tune (point: $x=3.78$ cm, $y=10.15$ cm and $z=220$ cm). These points correspond to the maximum temperature gradient near the water cooling channels. For comparison, the aluminum alloy 5083–H112 has yield strength of 193 MPa and fatigue strength of 158 MPa ($5 \cdot 10^8$ cycles).

1.5.3 Emergency in the corebox of the absorber

The emergency situation in the beam absorber arises when the primary proton beam will pass out of the target. It may happen in the cases, for example, when the current in the steering magnets of the proton beam line will be slightly different from the operation one, or the target is out of beam for some reason and so on. In such cases the proton beam with parameters given in Table 1.4 will strike on the corebox of the absorber.

Such situation was examined for one beam spill after long term continuous operation condition for 45 GeV/c tune, when the target by accidental way was out of beam. The results of the temperature calculations for this case are given in Figure 1.16. The temperature jumps are equal to 310°C and 26°C in graphite and in aluminum, respectively. The equivalent stress in the graphite section due to temperature jump reaches the value of 9.26 MPa (Figure 1.17a) and is rather small with respect to the strength limits for this graphite (see Table 1.1). The stresses in the aluminum section ($z=220$ cm) due to emergency spill (Figure 1.17b) are slightly higher

than those for operation conditions (see for comparison Figure 1.15b), but remain rather small with respect to yield stress limit of aluminum alloy used in the absorber.

1.6 Summary

The geometry of the beam absorber for narrow band neutrino beam was determined by the proton beam positions for various NBB tunes, as well as by the direction of neutral particles from the target. The distributions of incident energy on the absorber frontal face, as well as the energy deposition inside the absorber, have been calculated by MARS'96, widely used in the beam physics. The stresses and temperature computations have been made by program HAST well recommended at IHEP for a long time.

The proposed beam absorber design has sufficient temperature and stress safety factor to operate for a long period and may withstand a few emergency beam spills. It allows to absorb practically full incident energy and to defend the NBN magnet coils from radiation damage.

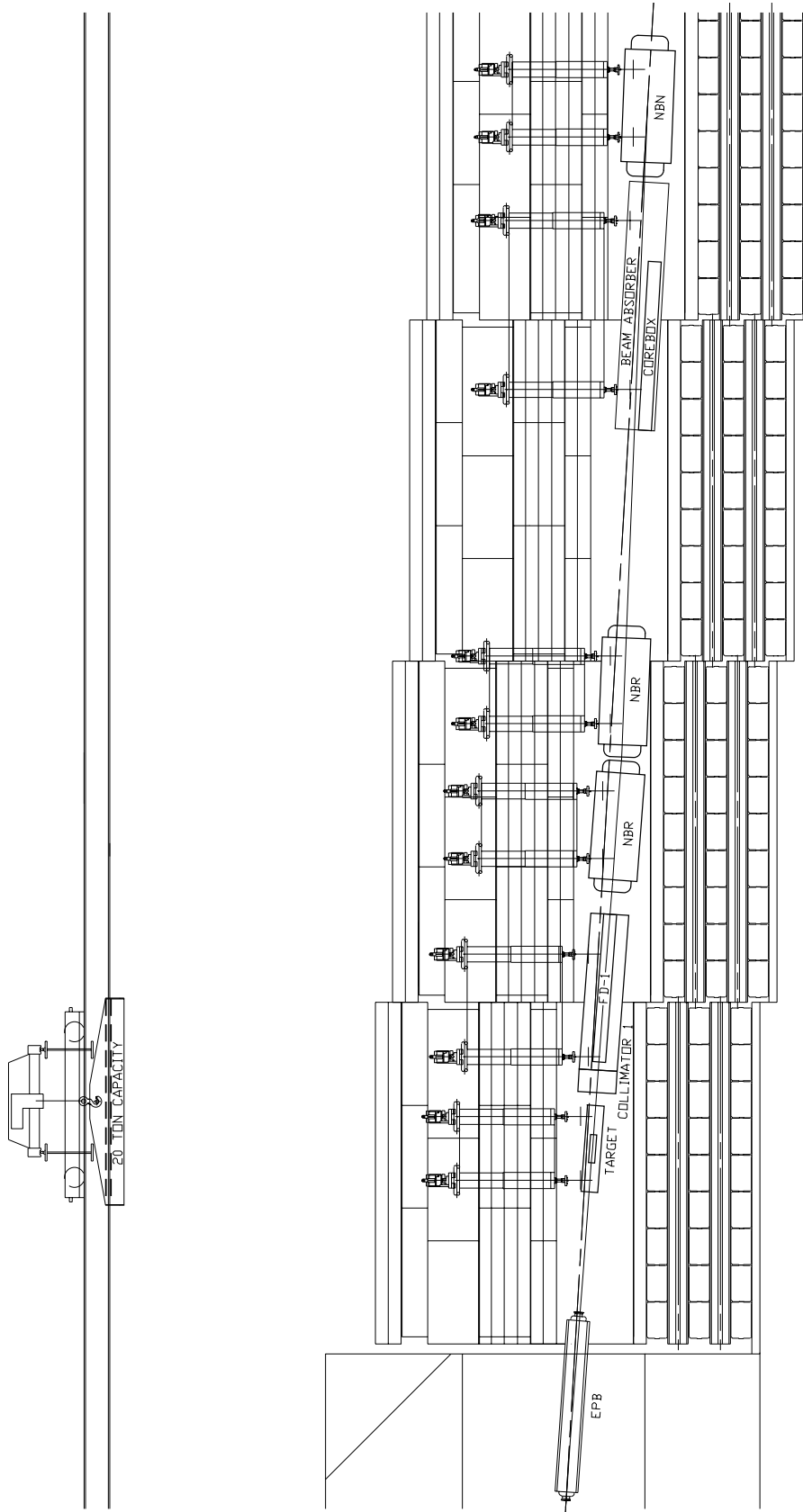


Figure 1.1: General view of the narrow band beam line.

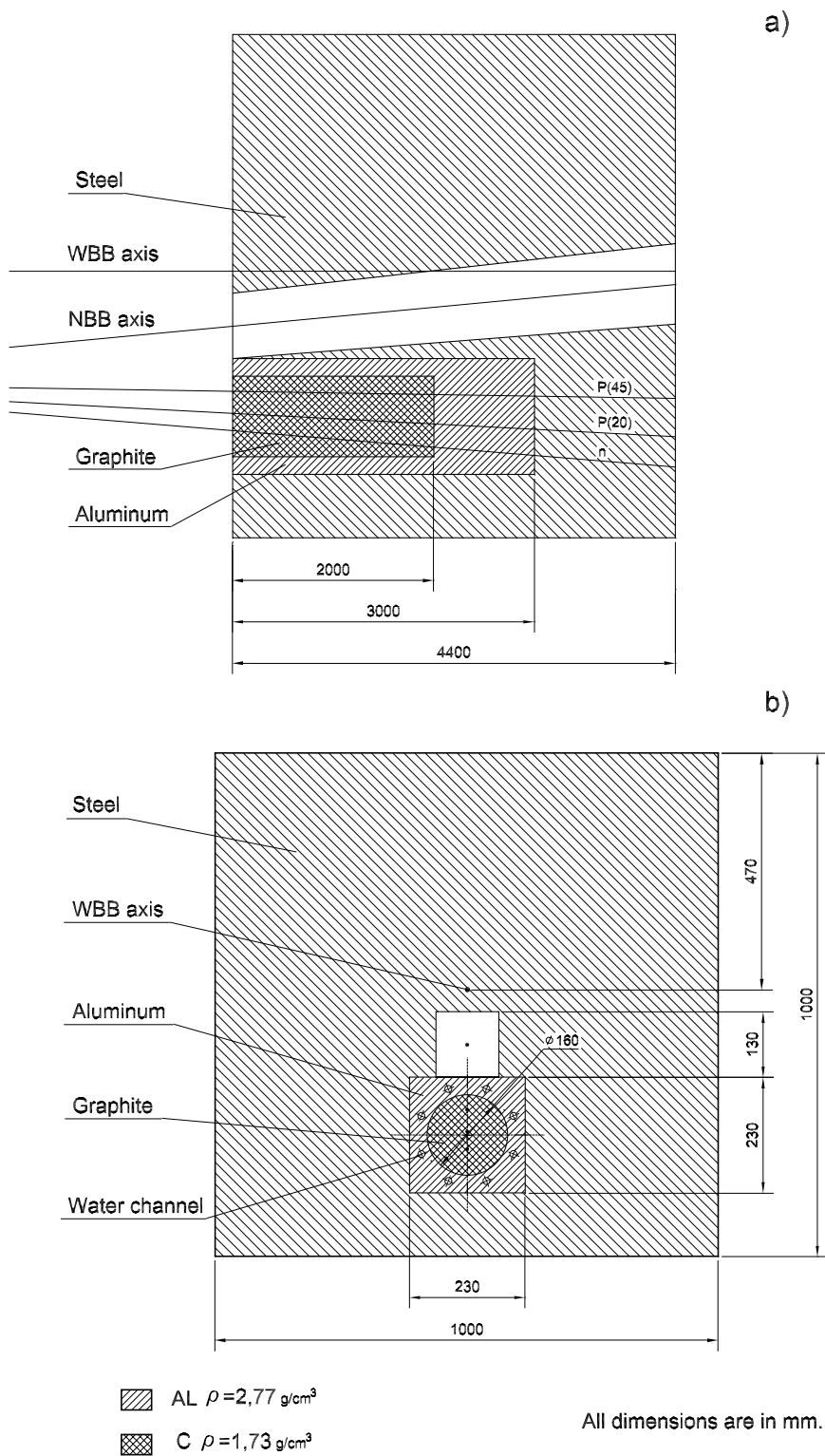


Figure 1.2: Longitudinal cross-section (a) and frontal view (b) of the NBB absorber.

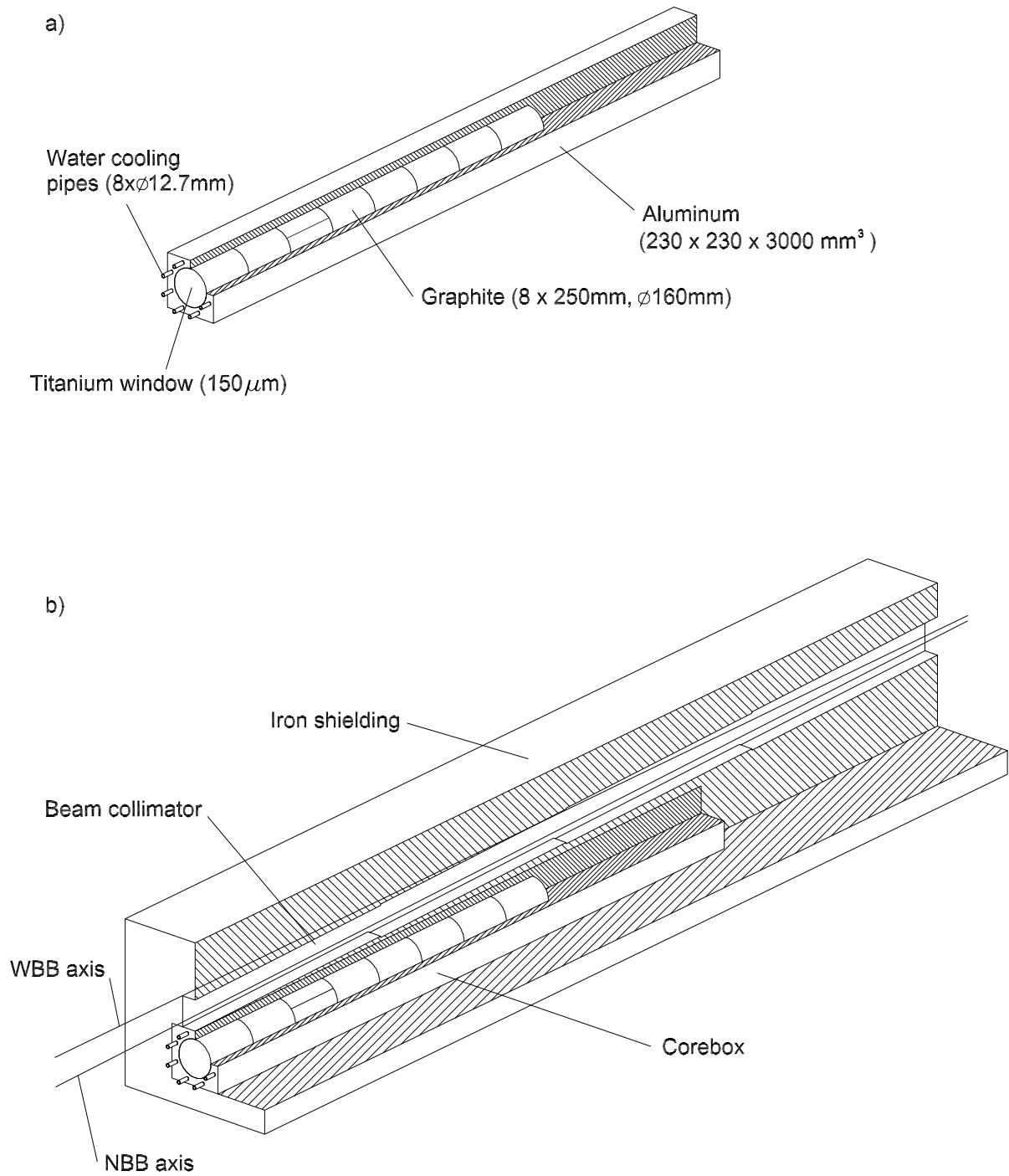


Figure 1.3: Cutaway isometrics of the absorber corebox (a) and absorber with a beam collimator (b).

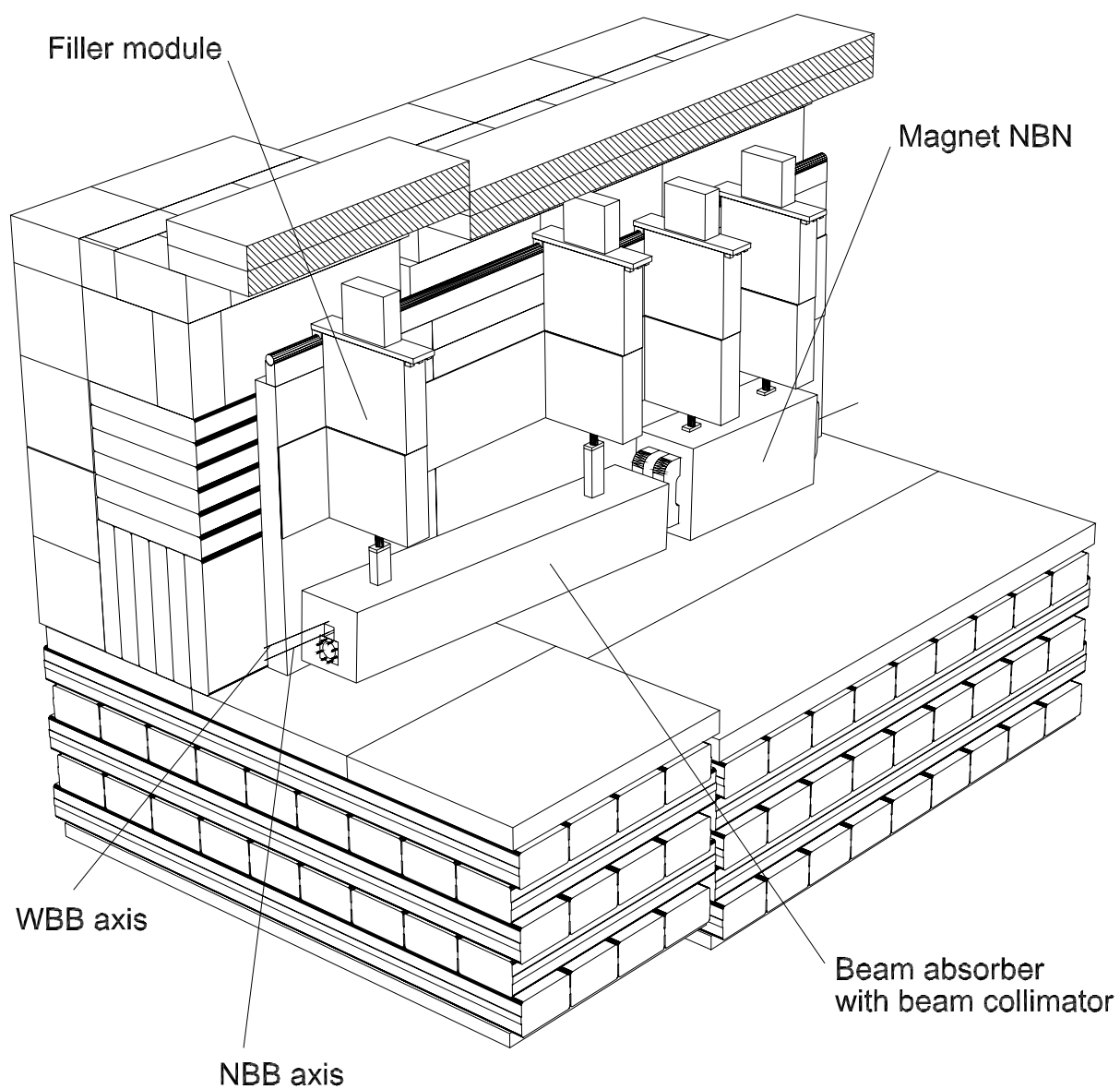


Figure 1.4: Perspective view of the absorber and NBN magnet in a beam line.

LONGITUDINAL DISTRIBUTION OF DEPOSITED ENERGY

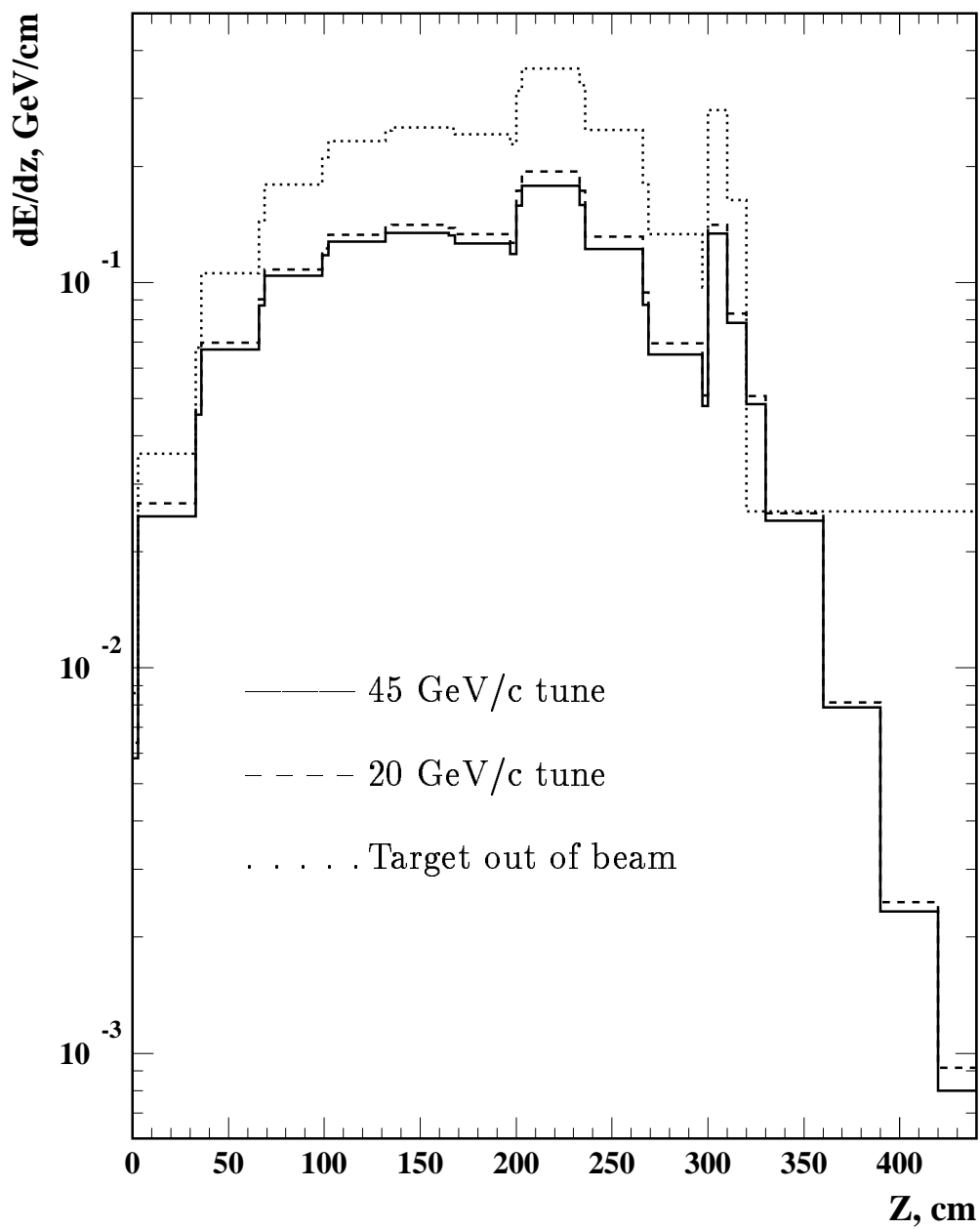


Figure 1.5: The longitudinal distribution of the energy deposited in the corebox.

MAXIMUM ENERGY DEPOSITION DENSITY

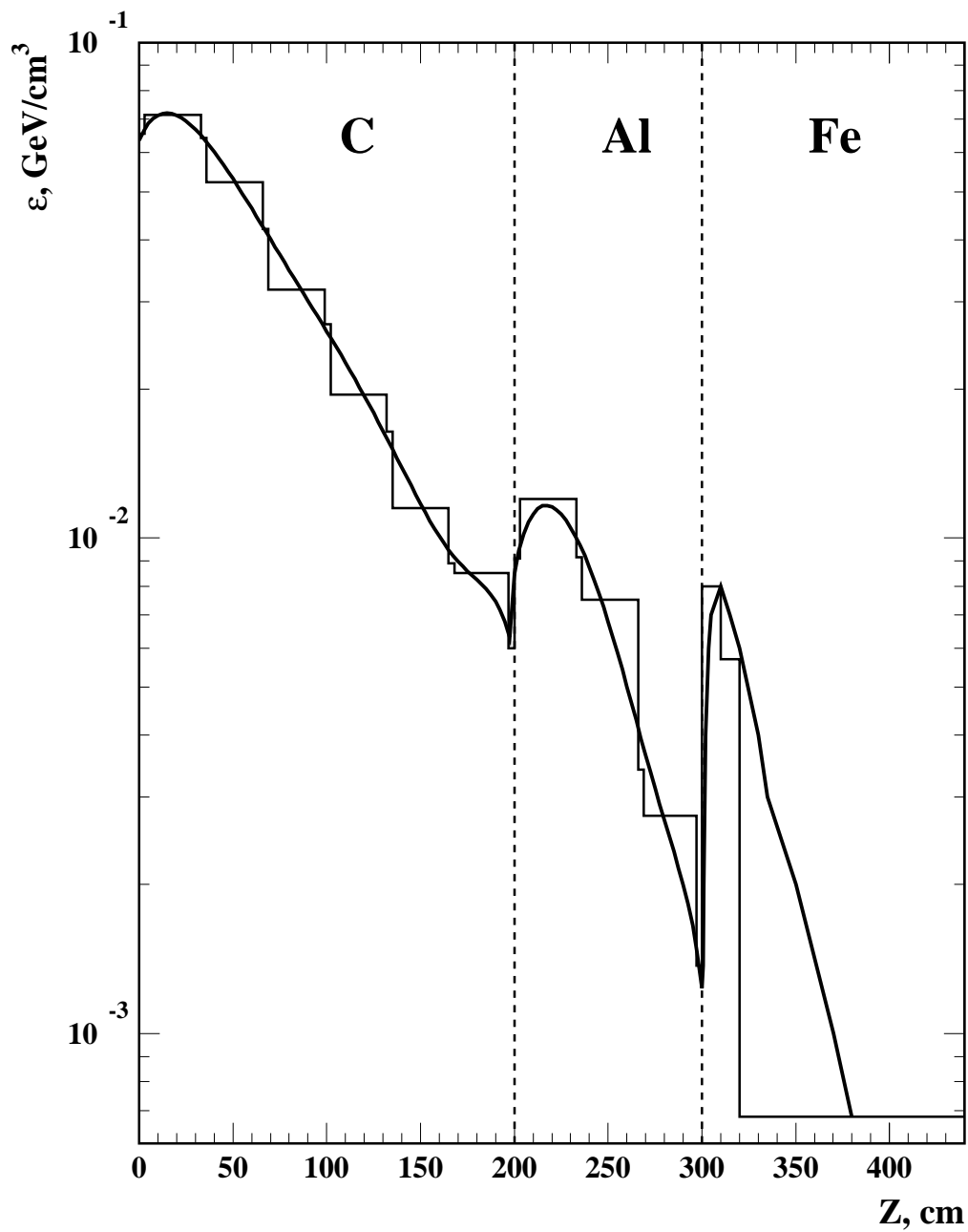


Figure 1.6: The longitudinal distribution of the maximum energy deposition density with the target out of beam.

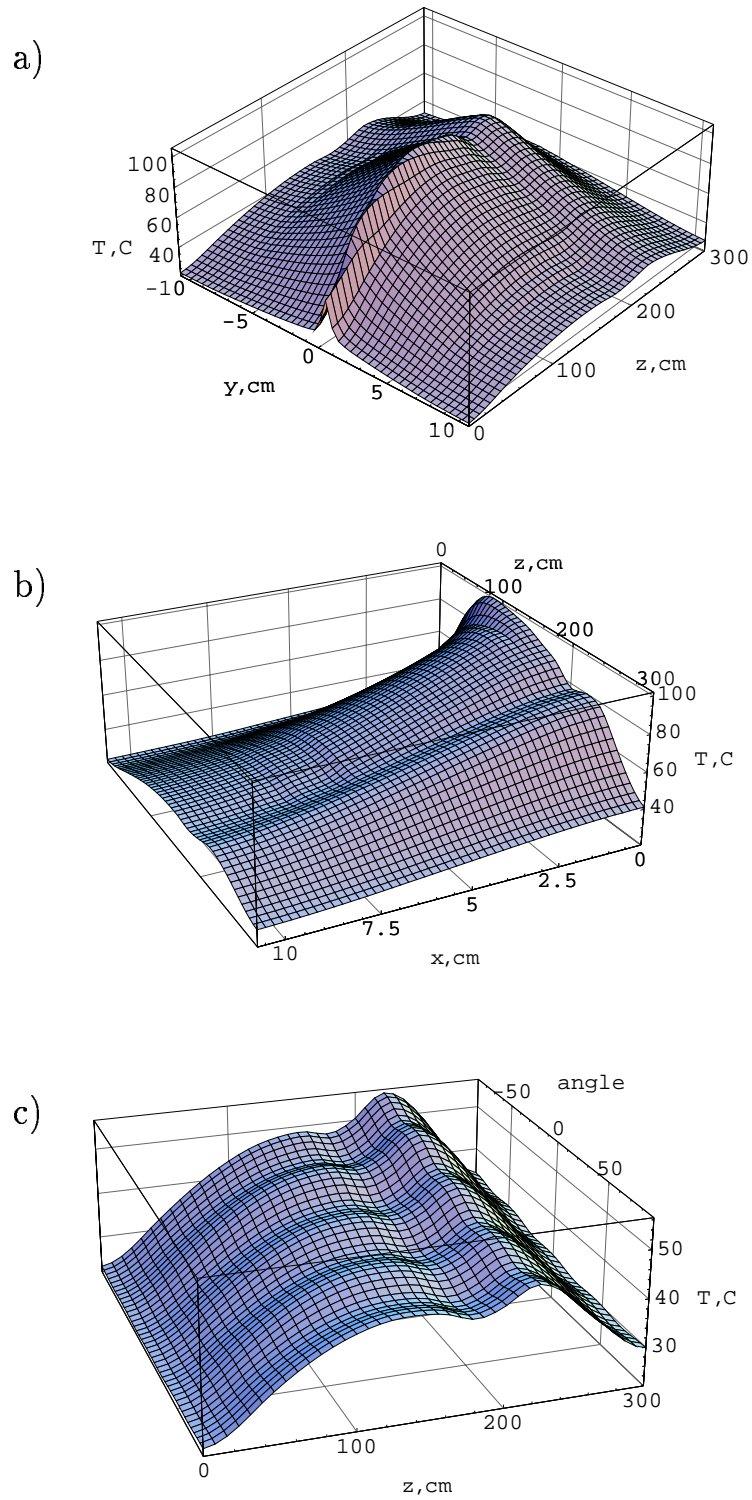


Figure 1.7: The temperature distributions in the absorber corebox after beam spill for the 20 GeV/c tune in ZY-plane at $x=0$ (a), in ZX-plane at $y=0$ (b) and along the graphite boundary (c).

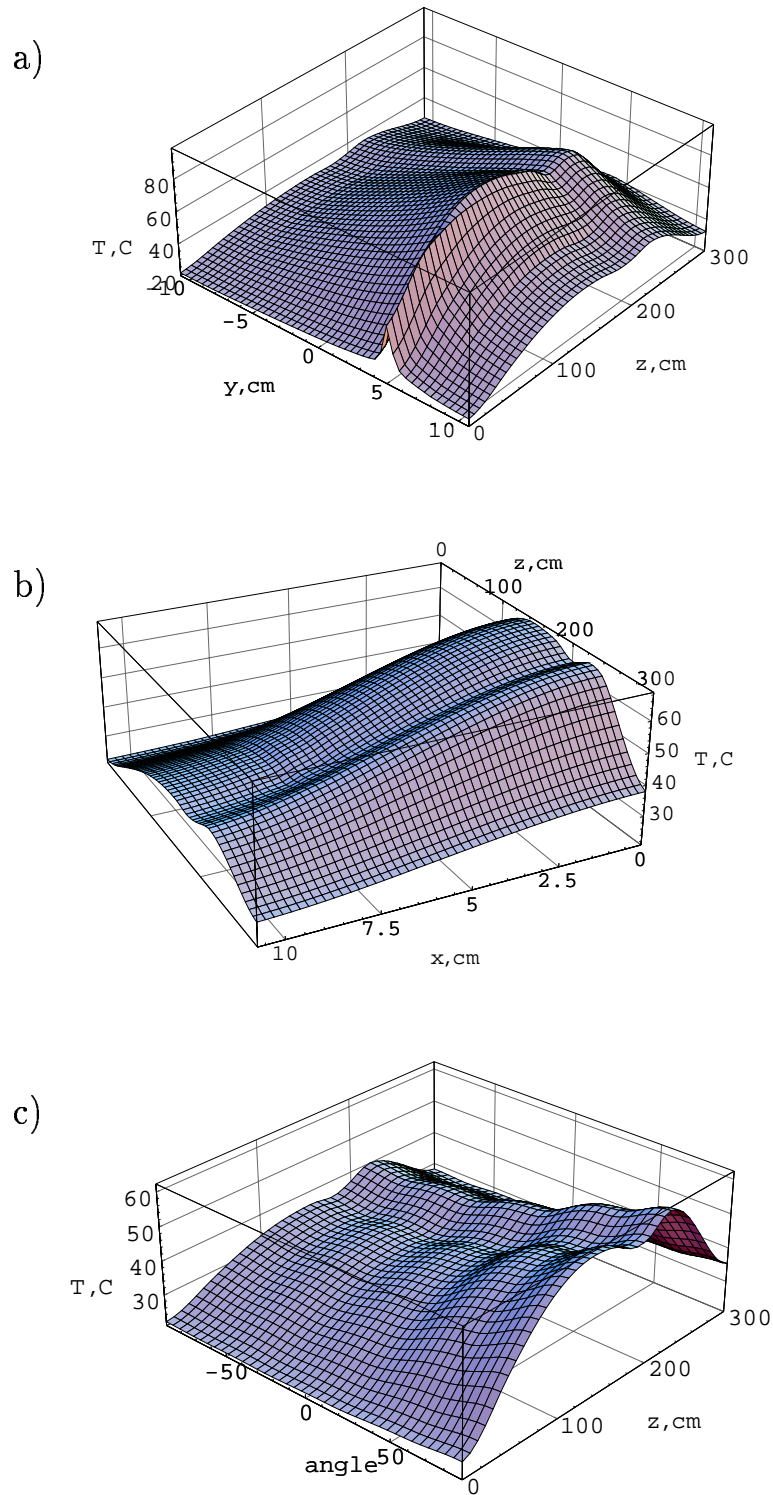


Figure 1.8: The temperature distributions in the absorber corebox after beam spill for the 45 GeV/c tune in ZY-plane at $x=0$ (a), in ZX-plane at $y=0$ (b) and along the graphite boundary (c).

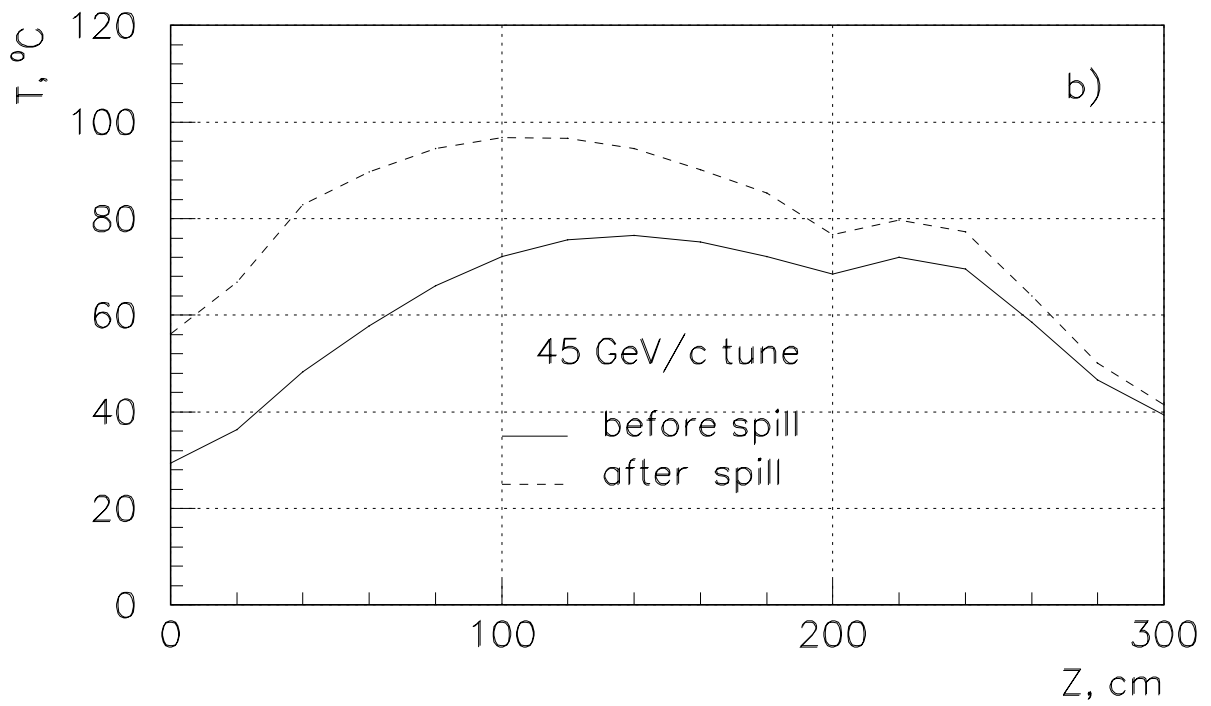
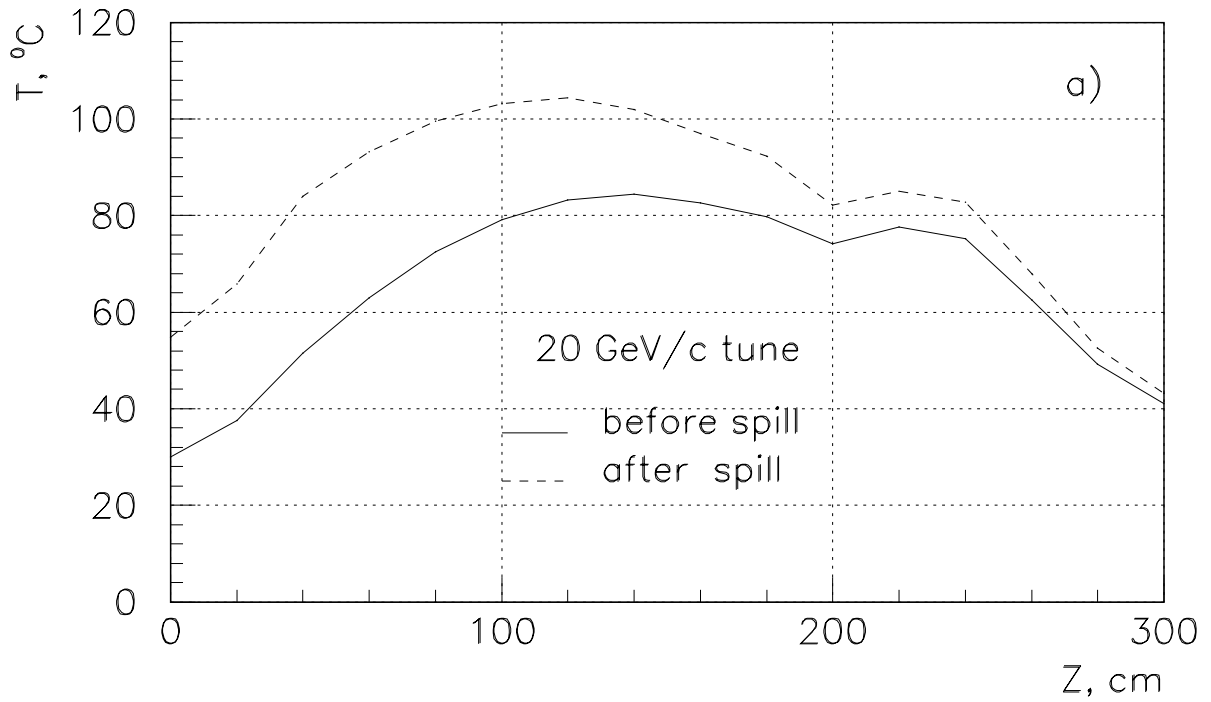


Figure 1.9: The temperature distributions along the beam axis as functions of azimuthal coordinate for 20 GeV/c tune (a) and 45 GeV/c tune (b).

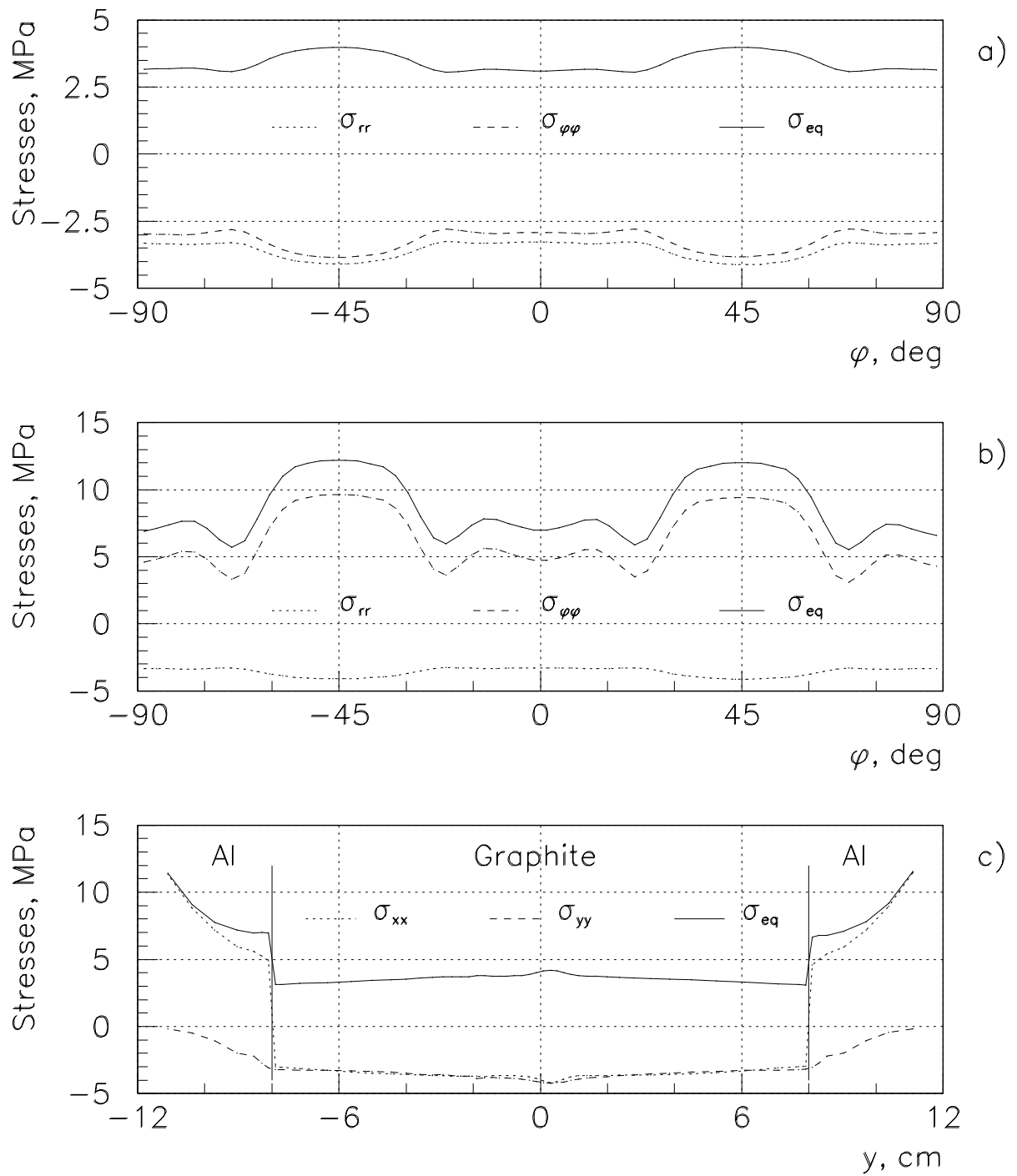


Figure 1.10: Stresses in the corebox graphite section at the cross-section of maximum density of deposited energy ($z=40$ cm) for 20 GeV/c tune: in graphite at $R=8$ cm (a), in aluminum at $R=8$ cm (b) and along the vertical axis at the symmetry plane $x=0$ (c).

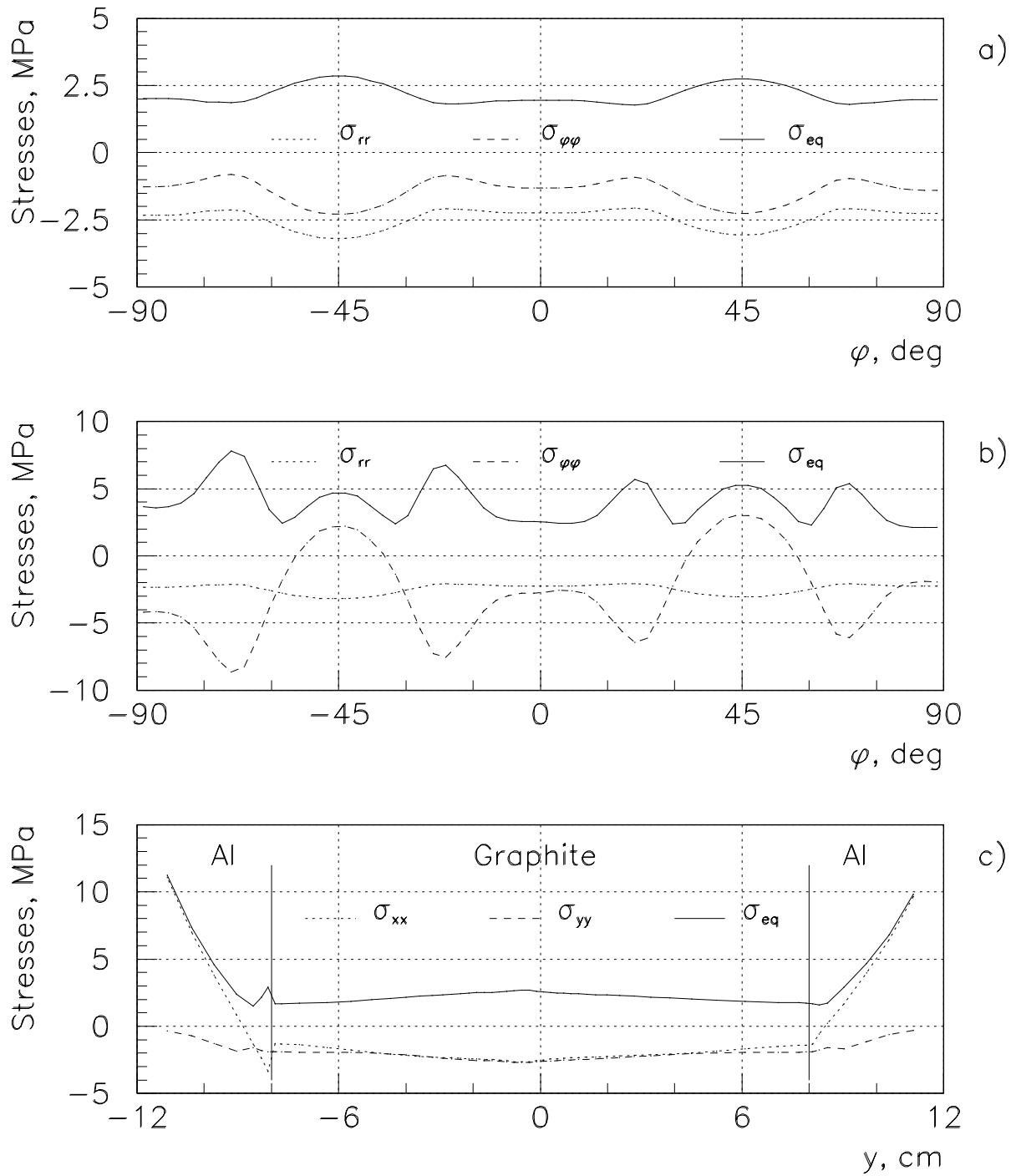


Figure 1.11: Stresses in the corebox graphite section at the cross-section of maximum deposited energy ($z=120$ cm) for 20 GeV/c tune: in graphite at $R=8$ cm (a), in aluminum at $R=8$ cm (b) and along the vertical axis at the symmetry plane $x=0$ (c).

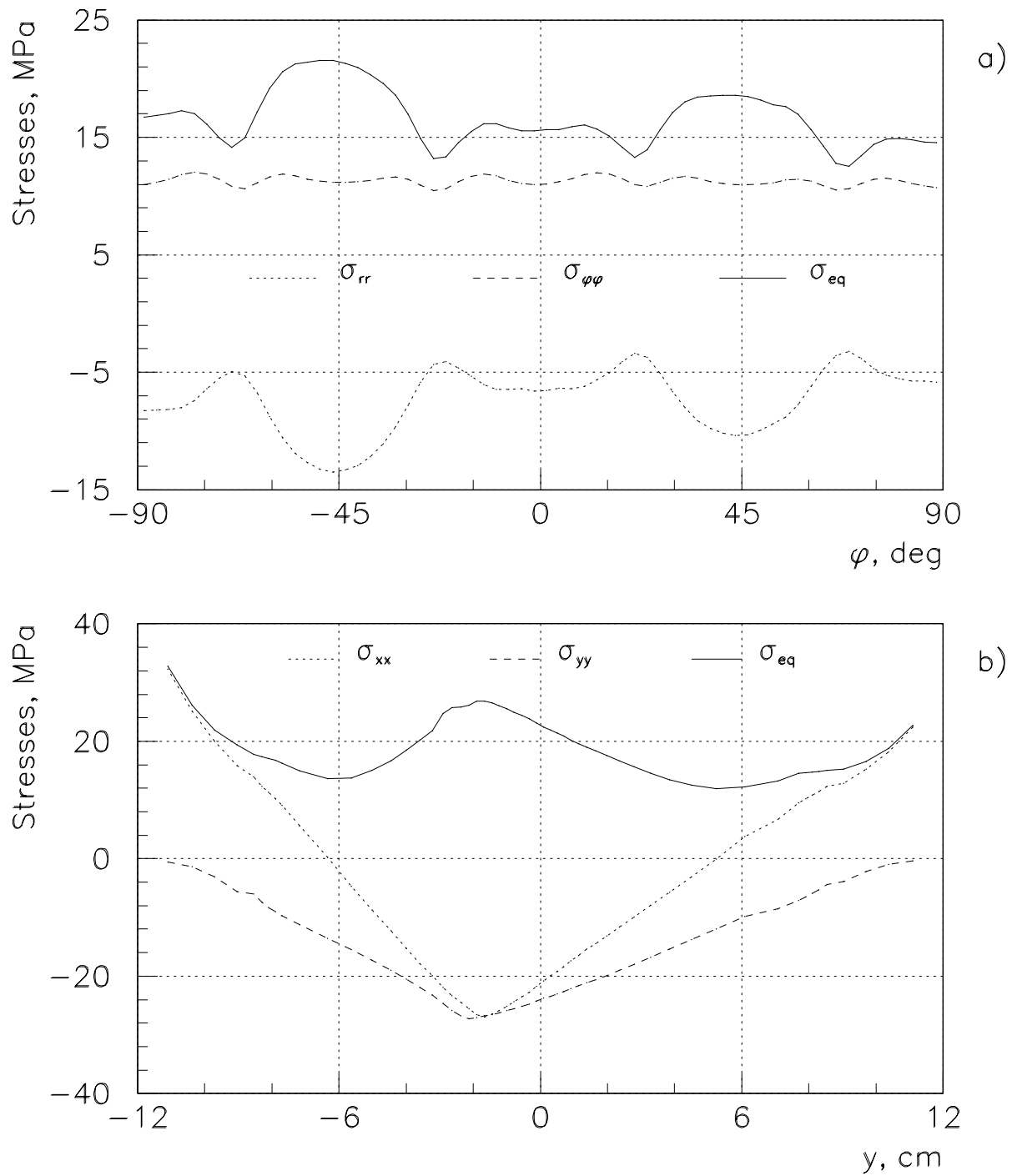


Figure 1.12: Stresses in the corebox aluminum section at the cross-section of maximum deposited energy ($z=220$ cm) for 20 GeV/c tune: at $R=8$ cm as function of angle (a) and along the vertical axis at the symmetry plane $x=0$ (b).

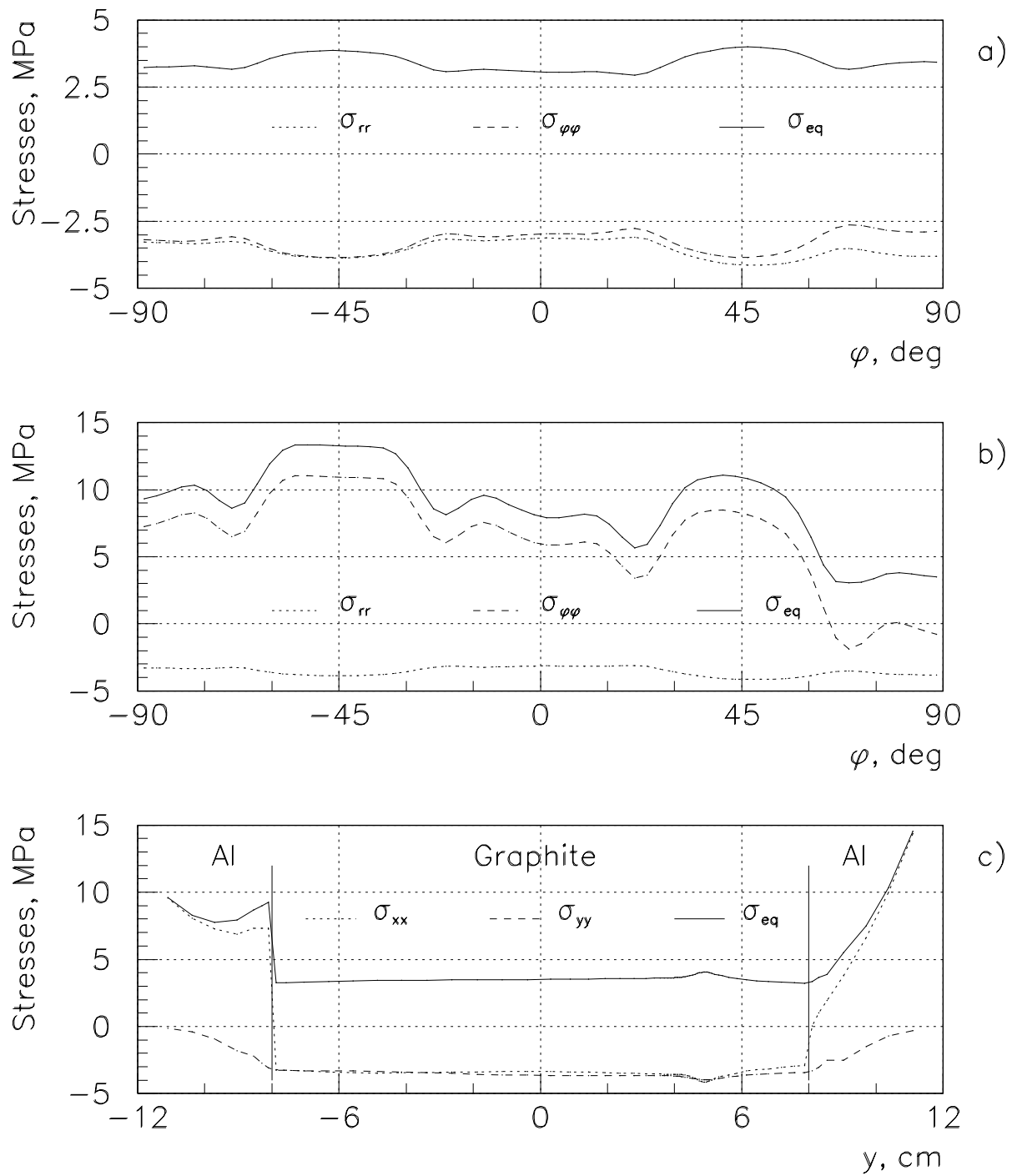


Figure 1.13: Stresses in the corebox graphite section at the cross-section of maximum density of deposited energy ($z=40$ cm) for 45 GeV/c tune: in graphite at $R=8$ cm (a), in aluminum at $R=8$ cm (b) and along the vertical axis at the symmetry plane $x=0$ (c).

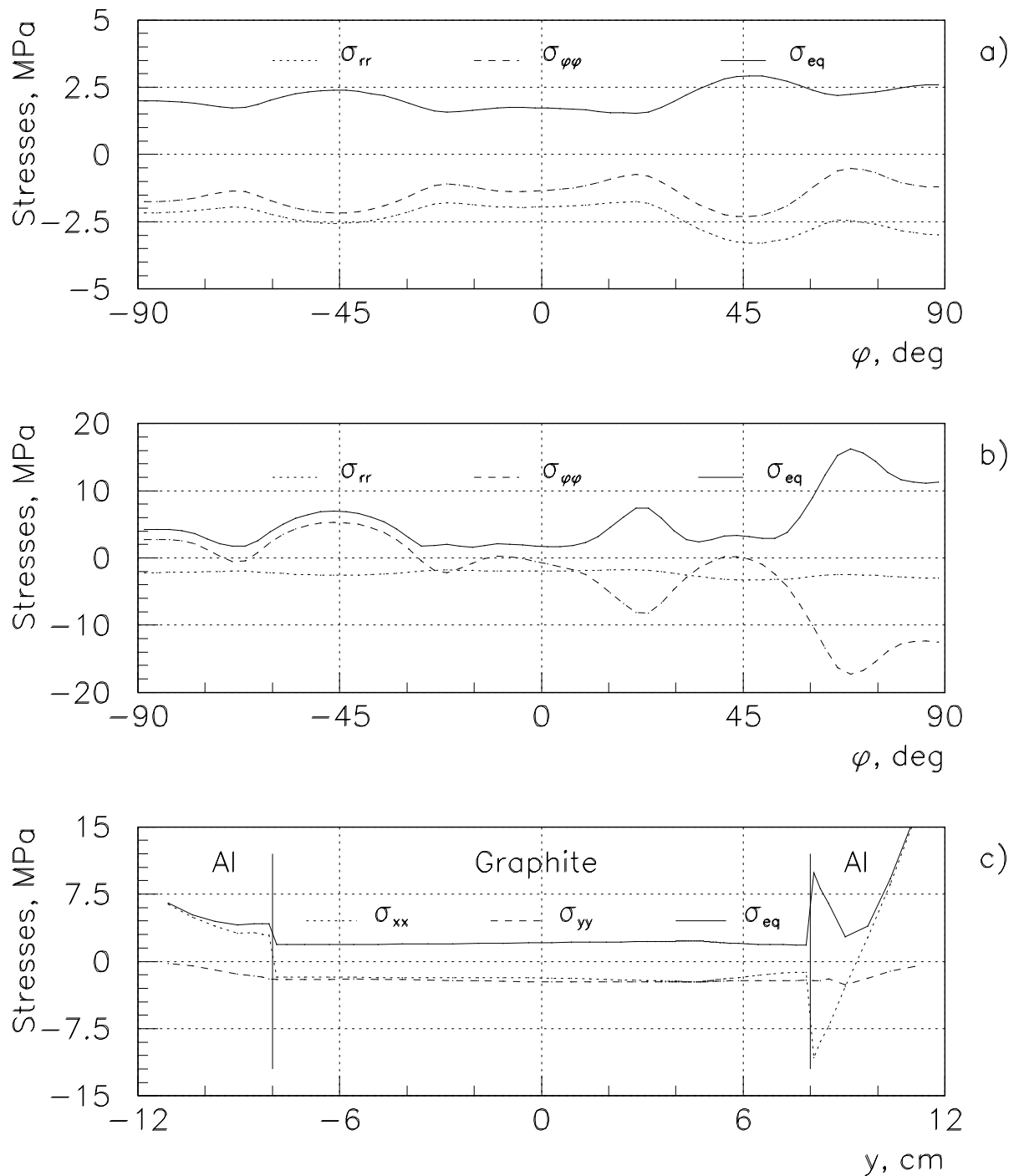


Figure 1.14: Stresses in the corebox graphite section at the cross-section of maximum deposited energy ($z=140$ cm) for 45 GeV/c tune: in graphite at $R=8$ cm (a), in aluminum at $R=8$ cm (b) and along the vertical axis at the symmetry plane $x=0$ (c).

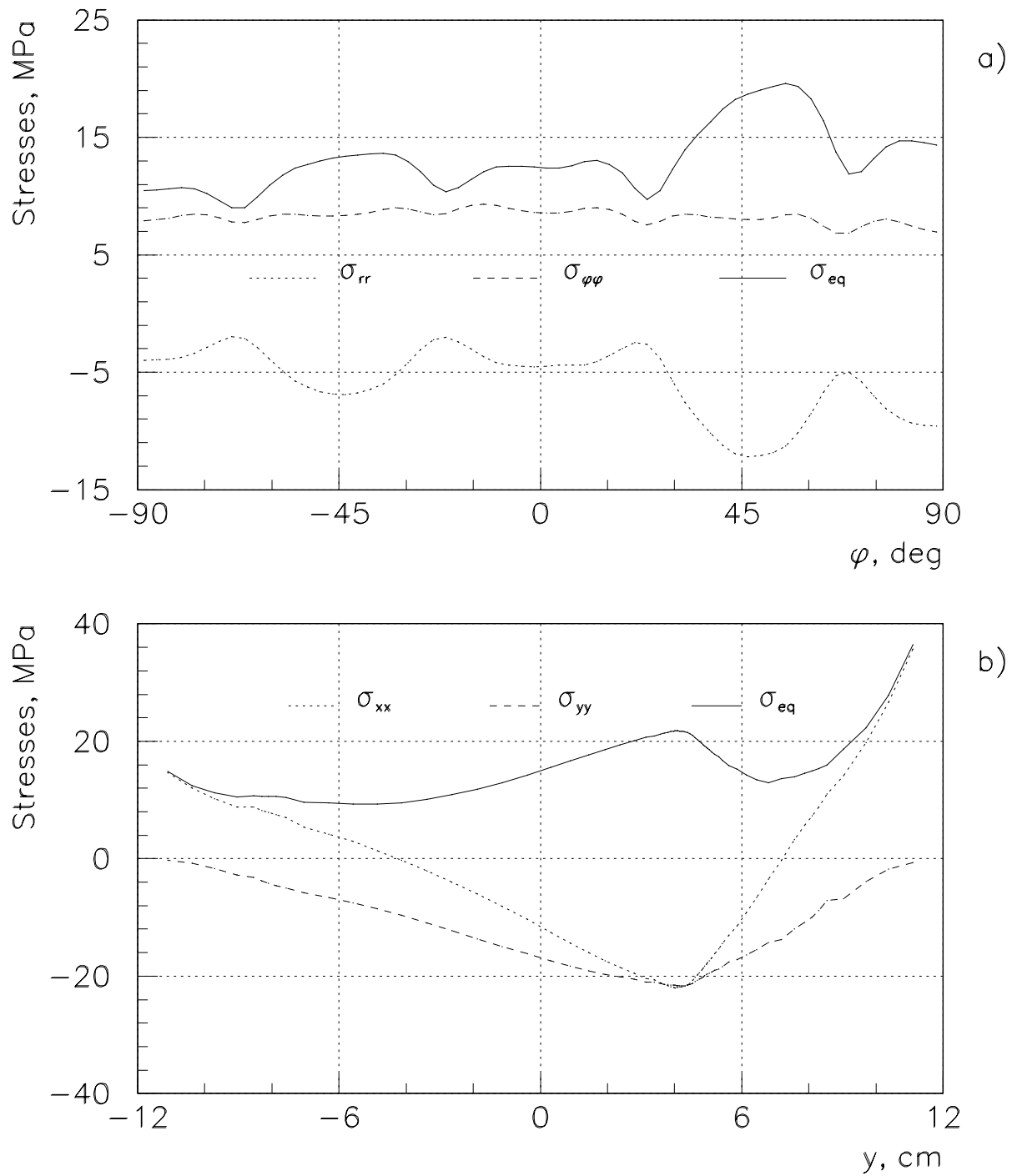


Figure 1.15: Stresses in the corebox aluminum section at the cross-section of maximum deposited energy ($z=220$ cm) for 45 GeV/c tune: at $R=8$ cm as function of angle (a) and along the vertical axis at the symmetry plane $x=0$ (b).

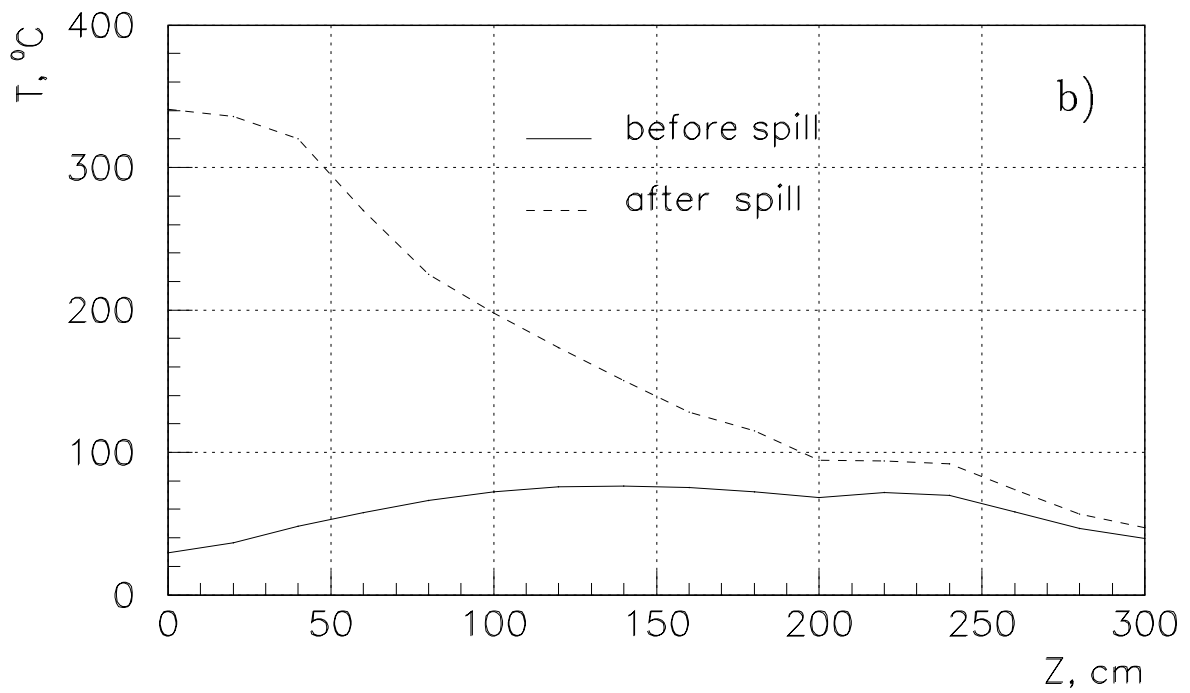
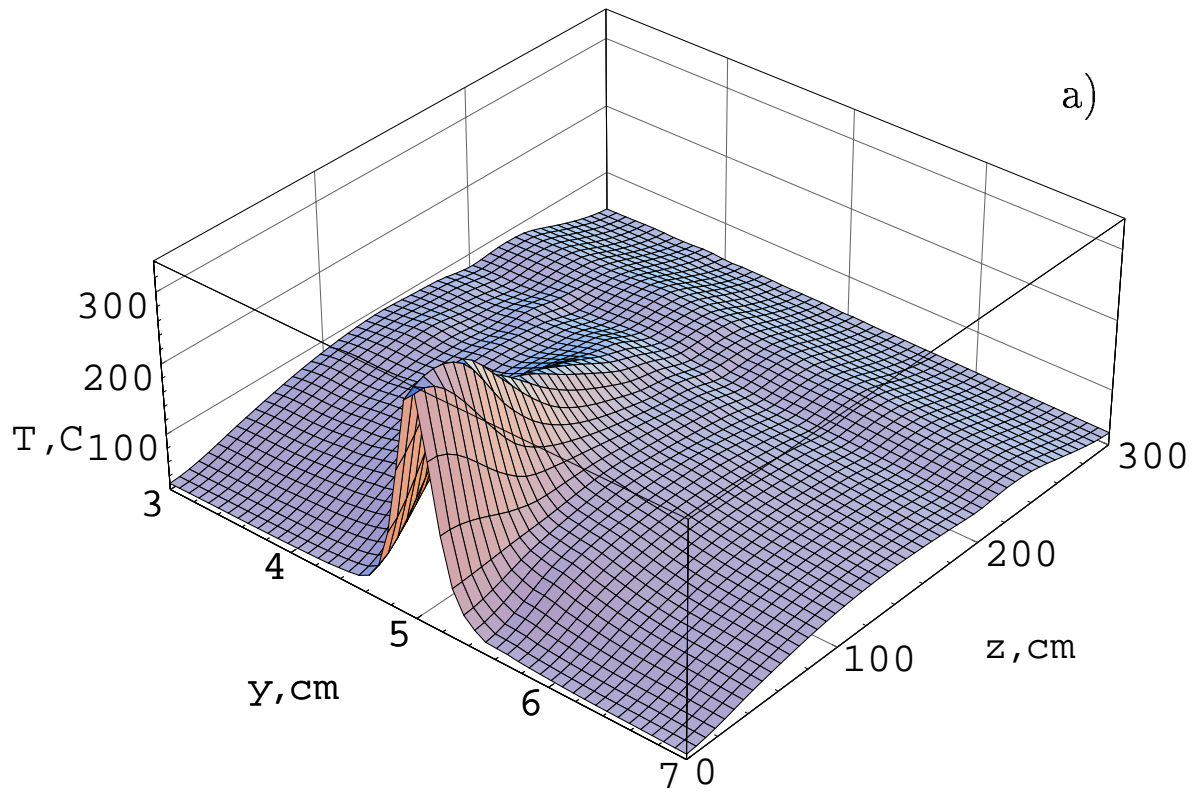


Figure 1.16: The temperature distributions in the absorber corebox after one beam spill without the target for 45 GeV/c tune in ZY-plane at $x=0$ (a) and along the beam axis as function of azimuthal coordinate (b).

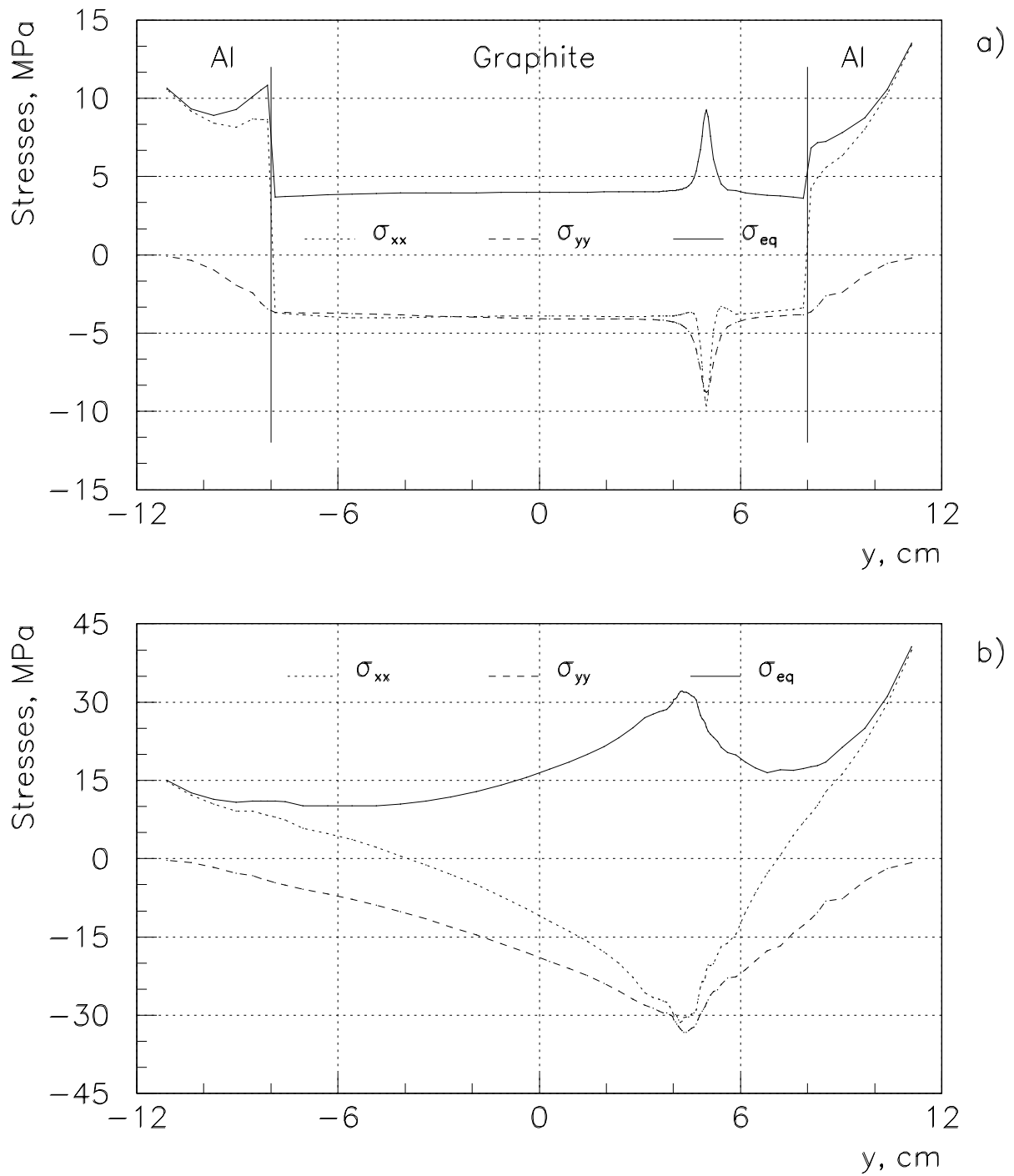


Figure 1.17: The maximum stresses in the corebox along the vertical axis in the symmetry plane $x=0$ for one beam spill without the target for 45 GeV/c tune in graphite section at $z=20$ cm (a) and aluminum section at $z=220$ cm (b).

2 Low Energy Wide Band Beam

The H6.6 focusing system consisting of three conical horns has been investigated in Fermilab [6] to produce a wide band beam (WBB) in neutrino energy range of 8–25 GeV at the detectors located 1.3 km (near) and 732 km (far) downstream the target. This beam, which will use 120 GeV primary protons from the Fermilab Main Injector now under construction, is designed for the discovery and subsequent study of the phenomena of neutrino oscillations over a wide range in the Δm^2 – $\sin^2 2\theta$ plane. Since the probability of oscillations goes as

$$P_{\nu_a \rightarrow \nu_b} = \sin^2 2\theta \cdot \sin^2 \left(1.27 \Delta m^2 \frac{L}{E_\nu} \right),$$

where $\Delta m^2 = |m_{\nu_a}^2 - m_{\nu_b}^2|$ in eV^2 , L in km and E_ν in GeV, the WBB with a lower neutrino energy would be desired to extend the lower end of the Δm^2 range for the same neutrino detector location.

So far as the improvement of the low energy performance of the H6.6 design is contrary to a relatively small radius of its first horn, a focusing system with larger radius of the first horn is needed for the effective collection of the pions which would give the low energy neutrinos. In addition, a new study of horn shapes and their location, as well as appropriate changes in the target design are also required.

This Section presents the results of conceptual study of the focusing system for the low energy WBB, which would enhance the neutrino event rate at the far detector with respect to the current baseline design H6.6 in the energy range of $E_\nu < 12$ GeV.

2.1 Focusing Systems

Two types of horns with different shapes of inner conductors have been considered as possible focusing devices for the low energy WBB. The horn with the conical shaped inner conductor focuses secondary particles of the same transverse momentum p_t , whereas the horn with parabolic shaped inner conductor (parabolic lens) [7] focuses secondaries of all production angles for the particular momentum. To obtain a high intensity WBB in the wide range of neutrino energy, the focusing systems consisting of at least two focusing devices were taken into consideration.

The focusing systems with two parabolic horns (PH2) and three conical horns (CH3) have been optimized to produce at the far detector the WBB with neutrino energy less than 12 GeV. Figure 2.1 shows the schematics of the PH2 and CH3 low energy (LE) focusing systems. The main geometrical parameters of parabolic and conical horns being used in the PH2 and CH3 designs are given in Figures 2.2 and 2.3. The horn currents in both focusing systems are equal to 200 kA.

The first horn neck radius is essentially smaller than that for the subsequent horns in both focusing systems. In order to limit the neck temperature jump due to the peak power by the value of 25°C, the inner conductors in the neck region of the first horns were chosen 4.5 mm in thickness. The wall thickness of the first horns decreases continuously in the flange directions so that the cross-section of the inner conductor should not be smaller than that in the neck region. After the wall thickness reaches 2 mm, it remains constant up to the flanges. The inner conductor thickness for subsequent horns is equal to 2 mm in both focusing systems.

Electrical parameters of all horns being used in the LE focusing systems are listed in Table 2.1. The average power P , power flux from the neck surface and neck temperature jump ΔT were calculated assuming that $I(t) \sim \exp(-\alpha t) \sin(2\pi t/T)$, where $T=10$ ms with 1.9 s repetition period and α is defined only by the L and R parameters for each horn.

Parameters	PH2 Design		CH2 Design		
	Horn#1	Horn#2	Horn#1	Horn#2	Horn#3
Inductance L , nH	689	457	664	322	338
Resistance R , μOhm	316	112	285	92	66
Average power P , kW	17.5	7.5	16.1	5.9	4.8
Stored energy, kJ	13.8	9.1	13.3	6.4	6.8
	22.9		26.5		
Power flux from the neck surface, W/cm^2	11.2	4.7	11.4	3.3	1.9
Neck temperature jump ΔT , °C	22.8	18.4	23.2	13.0	7.3

Table 2.1: Electrical parameters of the horns.

To accept as many pions as possible, the graphite target with shorter length and higher density located close to the firsts horns was used for the low energy WBB instead of the two–interaction–length graphite target with "effective" density of $\sim 1.2 \text{ g/cm}^2$ (consisting of eight 12.5 cm long rods, each 0.2 cm in radius, separated by 8 cm long gaps) optimized for the H6.6 focusing system [8].

2.2 Neutrino Event Rates at the Far Detector

The neutrino event rate was calculated per one kiloton detector in one year, which assumes $3.7 \cdot 10^{20}$ protons on the target. The decay pipe 750 m in length and 1 m in radius embedded in these calculations has been optimized for the WBB in neutrino energy range of 8–25 GeV [9]. The results were obtained using Fermilab beam simulation software GNUMI which produces a weighted neutrino in the detector acceptance and includes a large number of physics effects. In particular, K^\pm , K_L^0 and μ^\pm decays gave the main contribution to the $(\nu_e + \bar{\nu}_e)$ background, and the production of secondaries in the horn and decay pipe walls was taken into account as well.

The ν_μ charged current event rates at the far detector as functions of the neutrino energy for the PH2 and CH3 focusing systems in comparison with the event rate for the H6.6 design are shown in Figure 2.4. The ratios of the PH2 and CH3 spectra to the H6.6 spectrum are given in Figure 2.5. The total ν_μ charged current event rates for these focusing systems in different neutrino energy ranges are listed in Table 2.2.

Focusing systems	Number of ν_μ events per kTon·Yr in the energy range of (GeV)			
	3–9	4–12	5–15	0–50
H6.6	525 (1.00)	1036 (1.00)	1510 (1.00)	3753 (1.00)
PH2	956 (1.82)	1045 (1.01)	970 (0.64)	1476 (0.39)
CH3	895 (1.70)	1365 (1.32)	1597 (1.06)	2189 (0.58)

Table 2.2: The ν_μ charged current event rates at the far detector in the different neutrino energy ranges.

Besides the differential distribution of the neutrino event rate dN/dE , an integral distribution $N(E) = \int_0^E \frac{dN}{dE} dE$ may be used to compare the focusing properties of different beam optics designs. The $N(E)$ curves for PH2, CH3 and H6.6 designs are shown in Figure 2.6. All curves are normalized so that 1.0 is the total neutrino event rate for the H6.6 design.

As follows from these results, the LE focusing systems PH2 and CH3 described in this Section significantly increase the neutrino event rate in the energy range of 3–9 GeV (factor 1.7–1.8) with respect to the H6.6 design. The PH2 focusing system is more effective in the energy range of 2–7 GeV than CH3 and gives the gain factors of 3.6, 2.7 and 1.7 to the H6.6 at neutrino energies of 3, 5 and 7 GeV, respectively. One should note that the increase of the neutrino event rate at low energies was obtained while the high energy component was reduced by an order of magnitude. As a result, the total ν_μ event rates in the full neutrino energy range for both LE designs are only 0.4–0.6 that for the H6.6.

The expected backgrounds at the far detector for the PH2 and CH3 focusing systems compared with those for the H6.6 one are given in Table 2.3. The most important background for oscillation experiments coming from the $(\nu_e + \tilde{\nu}_e)$ component tends to be larger for the LE designs (factor 1.8 and 1.4, for the PH2 and CH3 respectively). The main contribution to this background gives the electron neutrinos from K^+ and μ^+ three-body decays. Due to different decay angular distributions of the ν_μ and ν_e neutrinos in the laboratory frame the decrease of the ν_μ event rate at the far detector for the LE designs is accompanied by a non proportional decrease of the $(\nu_e + \tilde{\nu}_e)$ event rate and, as a result, by the rise of the $(\nu_e + \tilde{\nu}_e)$ background.

The defocusing of the negative pions travelling through the LE focusing system in the vicinity of the beam axis is not so effective as it is for the H6.6 design with smaller radius of the first horn. This leads to noticeable increase of the background from the $\tilde{\nu}_\mu$ component in the LE beams.

Contamination	H6.6	PH2	CH3
ν_μ	3753 (98.7%)	1476 (96.0%)	2189 (97.3%)
$\tilde{\nu}_\mu$	30.5 (0.80%)	47.0 (3.06%)	42.8 (1.90%)
ν_e	19.7 (0.52%)	14.1 (0.92%)	16.5 (0.73%)
$\tilde{\nu}_e$	0.66 (0.02%)	0.91 (0.06%)	0.87 (0.04%)

Table 2.3: Neutrino charged current event rates at the far detector.

2.3 Depth of Focus

The depth of focus is an important characteristic of the focusing system, which may be used to optimize the target length and density for different neutrino energy ranges. The depths of focus for the PH2 and CH3 focusing systems are shown in Figure 2.7. They were obtained by the event rate calculation at the far detector for different locations of the point-like target along Z -axis ($z=0$ corresponds to the upstream end of the first horn). The event rates in the neutrino energy ranges of 3–9, 4–12 and 5–15 GeV were taken into account, as well as ones in the full energy range. All curves are normalized so that 1.0 is the highest point of the curve for full neutrino energy range.

As follows from these plots, the target with a length of about 1.6 m is quite suitable to produce neutrino beam in the 5–15 GeV and higher energy ranges. A shorter and more dense target (about 1.0 m) will be better to produce neutrino beam in the low energy ranges. The maxima of the curves for different neutrino energy ranges are separated by 0.5–0.6 m for the PH2 focusing system, whereas for the CH3 focusing system this separation does not exceed 0.2–0.3 m. This means that the PH2 focusing system may be tuned to different neutrino energy ranges by changing the z -location of the target with respect to the first horn. In contrast, the focusing system CH3 which gave a wider neutrino spectrum (see Figure 2.4) is not so sensitive to the target position along Z -axis.

Figure 2.8 illustrates the possibility of neutrino energy range selection for the focusing systems being under consideration. The calculations were made for different graphite two-interaction-length targets, 2 mm in radius each. The T(1.0) "short" target is about 1 m in length with small gaps between segments (subsection 2.6), whereas the T(1.6) "long" target mentioned above has eight 12.5 cm long segments with 8 cm gaps between them.

The usage of the "long" target moves the neutrino spectra to a higher energy range by ~ 5.5 GeV for the PH2 focusing system and by ~ 2.8 GeV for the CH3 one. At the same time the total ν_μ charged current event rate increases by the factors of 1.6 and 1.3 respectively and reaches the values of 0.60 and 0.75 for the PH2 and CH3 focusing systems with respect to the H6.6 design. A further movement of the PH2 and CH3 neutrino spectra to a higher energy range by changing the target location only is not so effective as shown in Figure 2.8, and one needs other horn locations.

2.4 Decay Region

The total decay region length of 800 m (including 50 m target hall and 750 m decay pipe) and the decay pipe radius of 1.0 m which were used for the event rate calculations mentioned above, have been optimized for the WBB in neutrino energy range of 8–25 GeV [9]. Such decay regions parameters seem not quite optimum for the WBB in the energy range less than 12 GeV due to the larger parents beam dimension and divergence at the exit of the LE focusing system.

Figure 2.8 shows the variation in the total ν_μ charged current event rates at the far detector for various decay region lengths and decay pipe radii for the PH2 and CH3 low energy focusing systems. For a 800 m long decay region the event rate does not flatten out at the decay pipe radii less than 2.0 m. So, increasing the decay pipe radius from 1.0 m to 1.5 m it is possible to obtain 17% and 11% gains in the total event rate for the PH2 and CH3 focusing systems respectively. On the other hand, just the same event rate as one for the initial decay region parameters may be obtained by transforming the decay region to 600 m in length and 2.0 m in radius.

The ν_μ charged current event rates for the decay region parameters ($L=800$ m/ $R=1.5$ m) and ($L=600$ m/ $R=2.0$ m) are given in Figure 2.11 for the PH2 and CH3 designs in comparison with those for the initial decay region parameters ($L=800$ m/ $R=1.0$ m). As follows from these spectra, the main yield of extra neutrino events from an increase in the decay pipe radius goes to the 2–10 GeV energy range which coincides with the energy range for which both LE focusing systems are optimized.

2.5 Higher Energy Performance

As follows from the previous part of this Section, the horn parameters and their locations, as well as the target length, have been optimized for the WBB in neutrino energy range less than 12 GeV. More detailed consideration shows that the same horns may be used to obtain the WBB in a higher energy range covered by the H6.6 focusing system.

Besides the target displacement upstream the primary proton beam, another layout of the focusing devices is needed to form the parent particle beam with the momenta of 20–40 GeV/c. The total length of the focusing system should be increased up to 45–50 m to be compatible at the same time with the NuMI target hall configuration [8].

Table 2.4 gives the target and horns layouts for the PH2 and CH3 focusing systems discussed above, which were modified to produce a high energy neutrino beam. The ν_μ charged current event rates for these focusing systems calculated for 1.6 m long 2λ -target T(1.6) are shown in Figure 2.11. Both systems give neutrino spectra which are reasonably smooth for search of oscillatory effects. The total event rate reaches the value of 3380 for both PH2 and CH3 designs which is $\sim 9\%$ less than the H6.6 total event rate.

Focusing system	Element locations, m			
	Target	Horn#1	Horn#2	Horn#3
PH2	-3.4	0.0	40.0	—
CH3	-2.2	0.0	12.4	42.4

Table 2.4: The target and horns layouts for high energy tune of the PH2 and CH3 designs (locations are given for the upstream end of each element).

2.6 Target

The design of the short target T(1.0) used for the LE focusing systems mentioned above is similar to that described in [9]. One meter long target consists of eight ZXF-5Q graphite rods, each 12.4 cm in length and 4 mm in diameter. The gaps between the cylinders are equal to 1 mm which is sufficient to prevent their touch up at the temperature of $\sim 1000^\circ\text{C}$.

The energy deposition by the primary proton beam in the target has been calculated using MARS-13 [10] computer code for a circular beam spot size $\sigma_x = \sigma_y = 0.89$ mm. The energy deposition per one proton along the target is shown in Figure 2.12a. The maximum of the energy deposition is reached at $z = 10$ cm. The maximum energy deposition density on the axis is reached at the same part of the target and is equal to 0.075 GeV/g/proton. It corresponds to the maximum temperature rise of 420°C for the first proton beam spill with $4 \cdot 10^{13}$ protons.

The calculations of thermal stresses in a target caused by such temperature rise give the value of 32 MPa for quasistatic equivalent stress. This is a pessimistic estimation as the specific heat of ZXF-5Q graphite increases by a factor of 2 between the room temperature and 1000°C , while the product of the expansion coefficient and modulus of elasticity increases only by $\sim 60\%$.

The maximum and minimum (averaged over radius) temperatures at $z=10$ cm have been calculated as the functions of helium flow velocity (see Figure 2.12b) taking into account a radiative cooling and the dependence of the specific heat on the temperature. The value of 10 m/s seems to be quite reasonable for cooling of the most heated part of the target.

2.7 Summary

The focusing systems with two parabolic horns (PH2) and three conical horns (CH3) have been considered to produce at the far detector a WBB with neutrino energy $E_\nu < 12$ GeV (low energy WBB). The total horns lengths are equal to 6.0 m and 6.4 m for the PH2 and CH3 designs respectively; all horns in both focusing systems are filled in series by the current of 200 kA. The results of conceptual design of a low energy beam given in this Report show that:

- the focusing systems described here give more LE neutrinos with respect to the H6.6 three horn design. The gain factors of 3.6, 2.7 and 1.7 are reachable at the neutrino energies of 3, 5 and 7 GeV respectively, the total ν_μ charged current event rate is about 0.4–0.6 that for the H6.6 design;
- the most important background for oscillation experiments coming from electron neutrinos tends to be larger by a factor 1.4–1.8 for the LE designs;
- the target with shorter length and higher density, as well as decay pipe with larger radius are preferable for the LE beams;
- the tune to different neutrino energy ranges is possible by changing a target location along z -axis with respect to the first horn. Both focusing systems may be rearranged (by changing the target and horn locations) to obtain a "high energy" neutrino beam in the energy range covered by the H6.6 design;
- the parabolic horns of the PH2 design with the same power supply system, and with addition of some dipoles, collimators and primary proton beam dump, give the possibility to have the narrow band neutrino beam. More detailed calculations are needed to obtain the parameters of such beam.

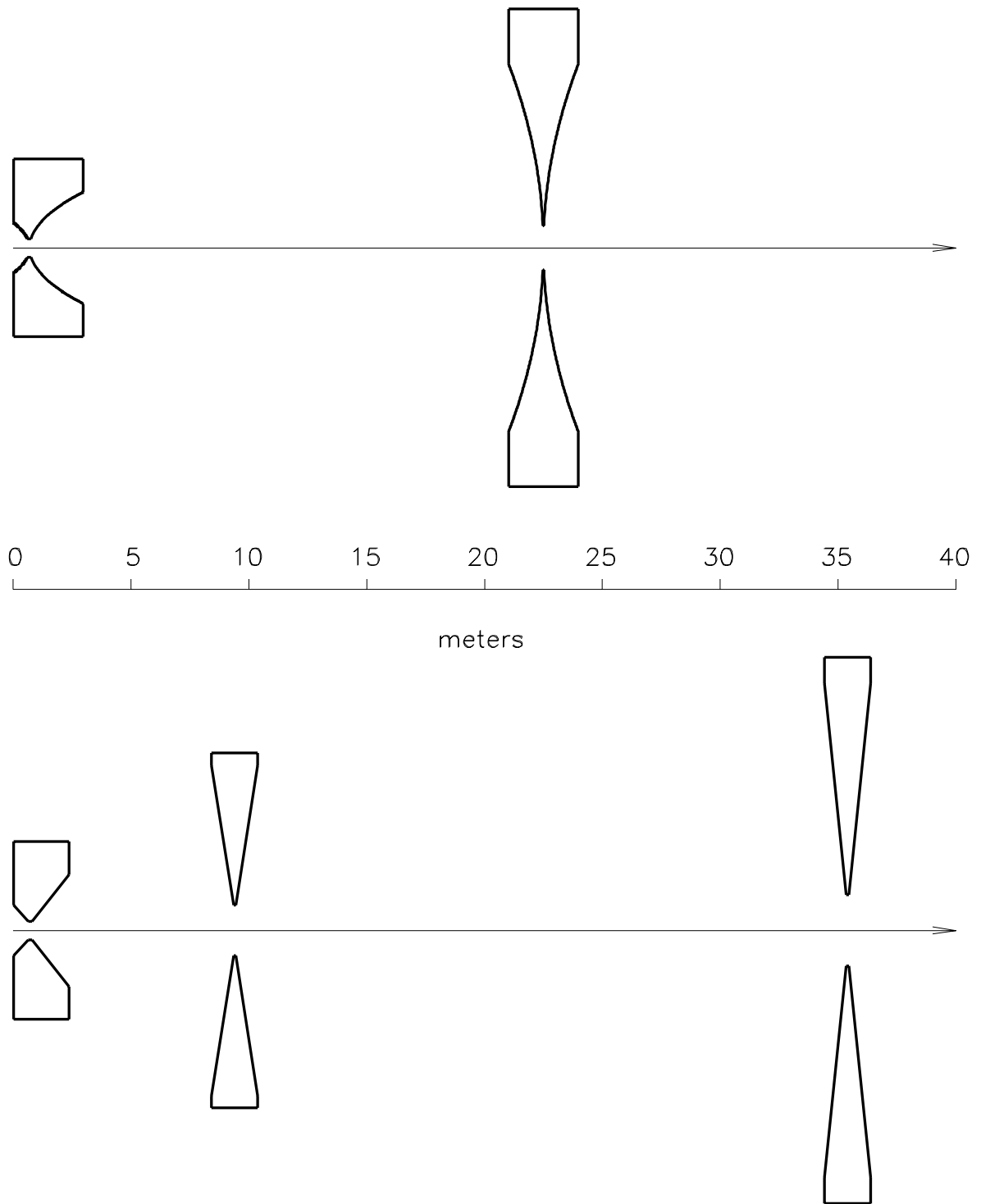
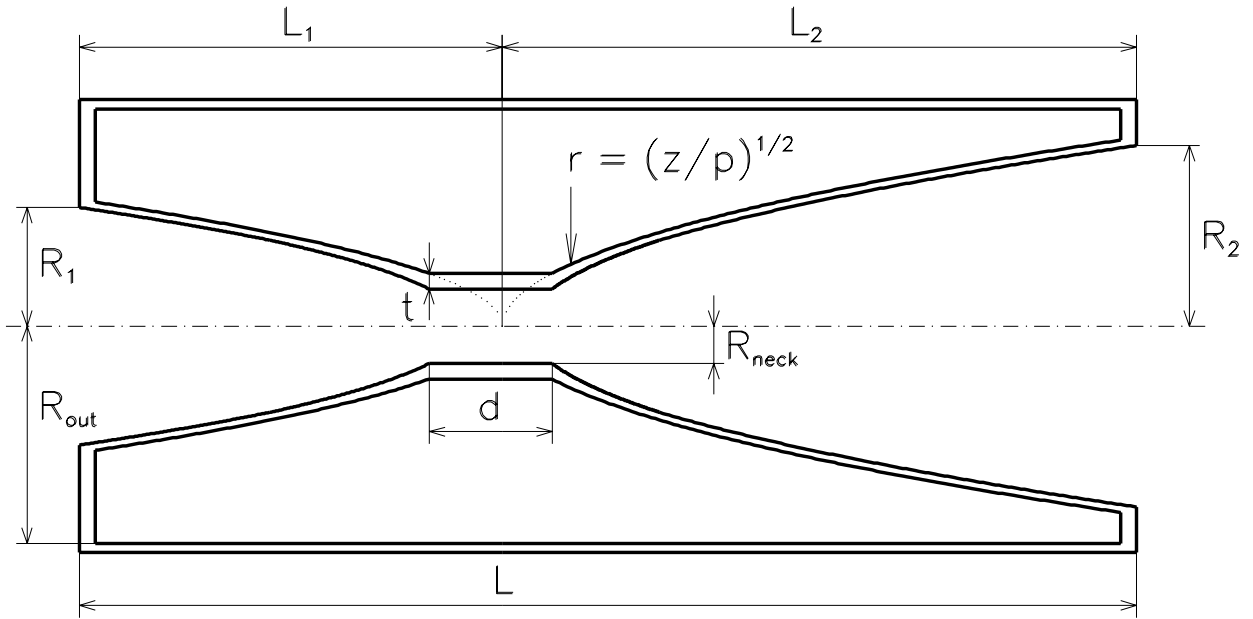
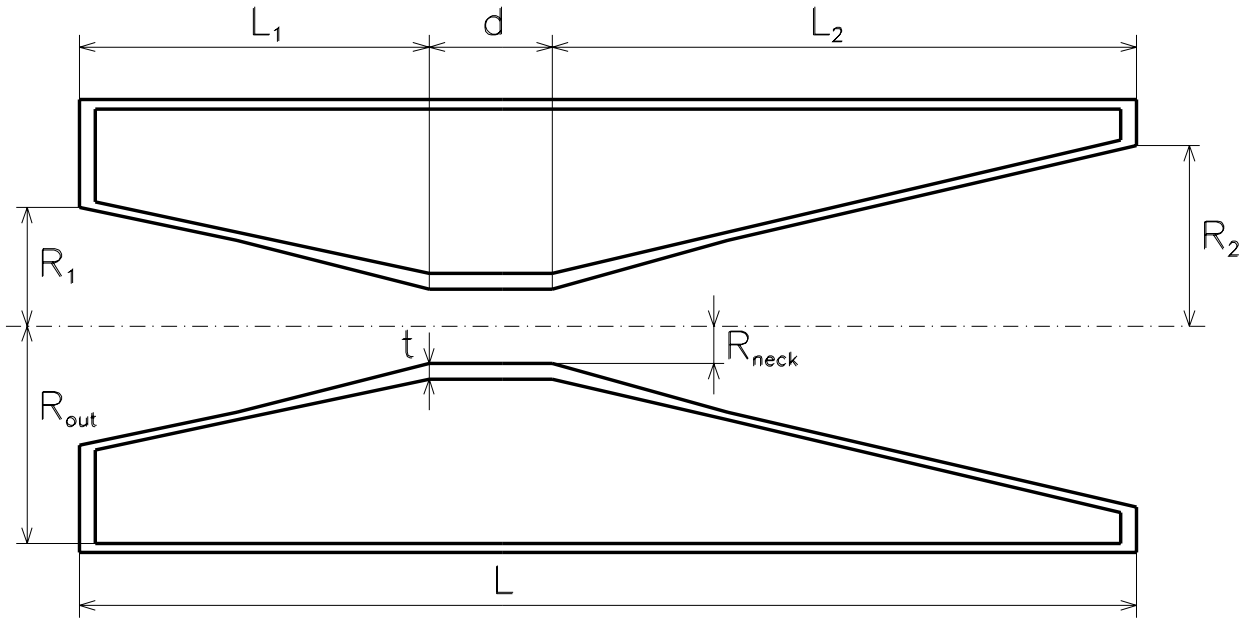


Figure 2.1: Schematics of the PH2 (top) and CH3 (bottom) designs.



Parameters	Horn#1		Horn#2
	1-st part	2-nd part	
Location, m	0		21.0
L, cm	300		300
d, cm	15.31		4.17
R _{out} , cm	13		35
R _{neck} , cm	0.9		3.0
t, mm	4.5		2.0
L ₁ , L ₂ , cm	70	230	150
R ₁ , R ₂ , cm	3.54	8.03	27.14
p, cm ⁻¹	5.0	3.4	0.2

Figure 2.2: Horn parameters for the PH2 two parabolic horns design (locations are given for the upstream end of each horn).



Parameters	Horn#1		Horn#2	Horn#3
	1-st part	2-nd part		
Location, m	0		8.4	34.4
L, cm	240		200	200
d, cm	15		10	10
R_{out} , cm	13		26	40
R_{neck} , cm	0.9		3.5	5.0
t, mm	4.5		2.0	2.0
L_1, L_2 , cm	65	160	95	95
R_1, R_2 , cm	3.5	8.0	24	36

Figure 2.3: Horn parameters for the CH3 three conical horns design (locations are given for the upstream end of each horn).

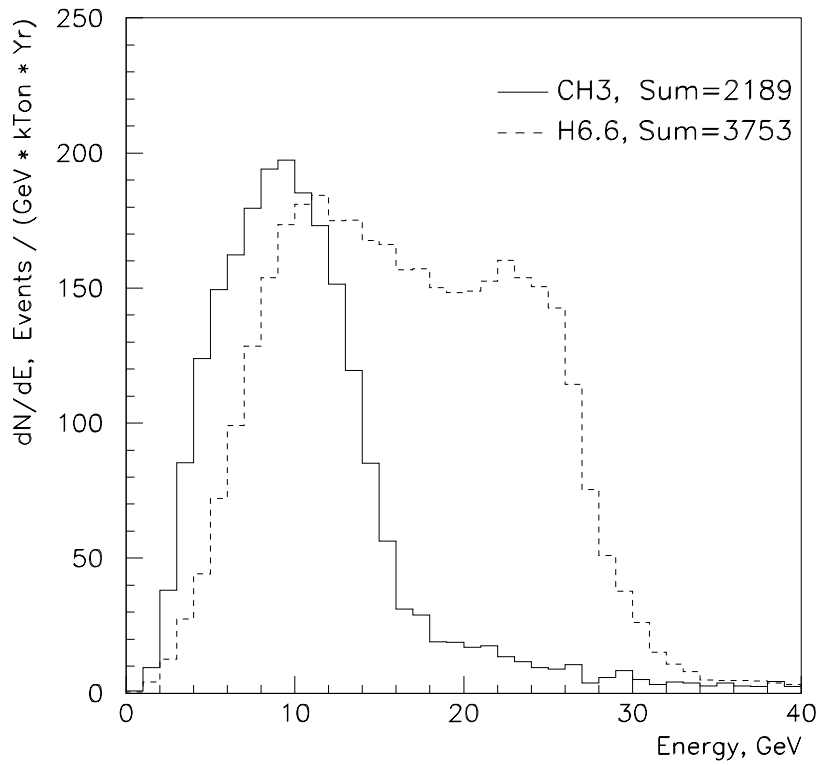
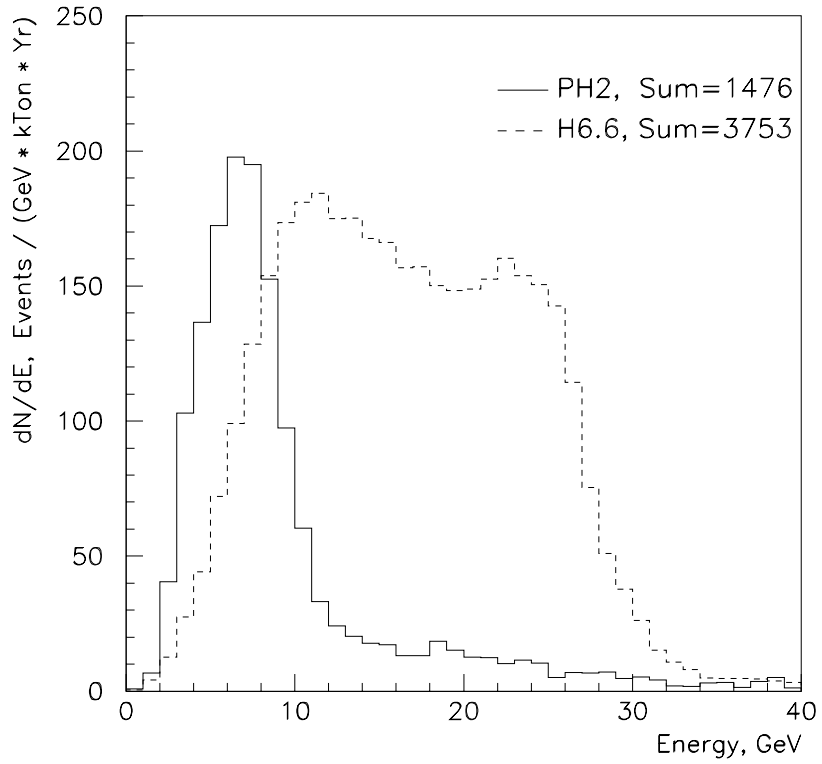


Figure 2.4: The ν_μ charged current event rates for the PH2 and CH3 designs.

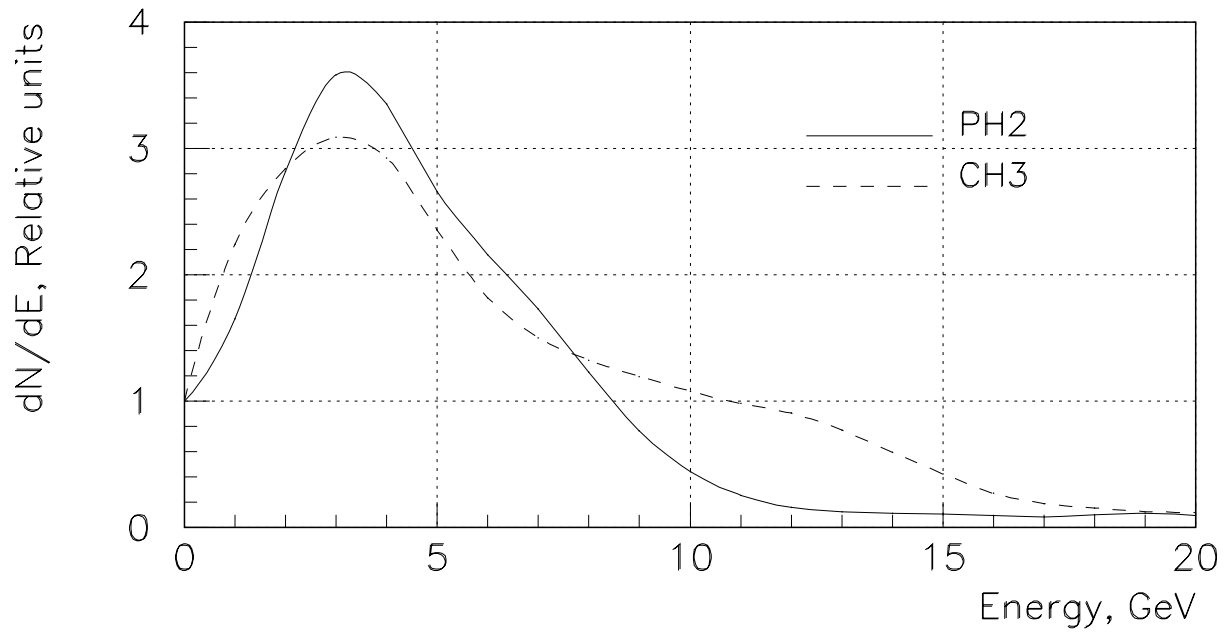


Figure 2.5: The ratios of the PH2 and CH3 spectra to the H6.6 spectrum.

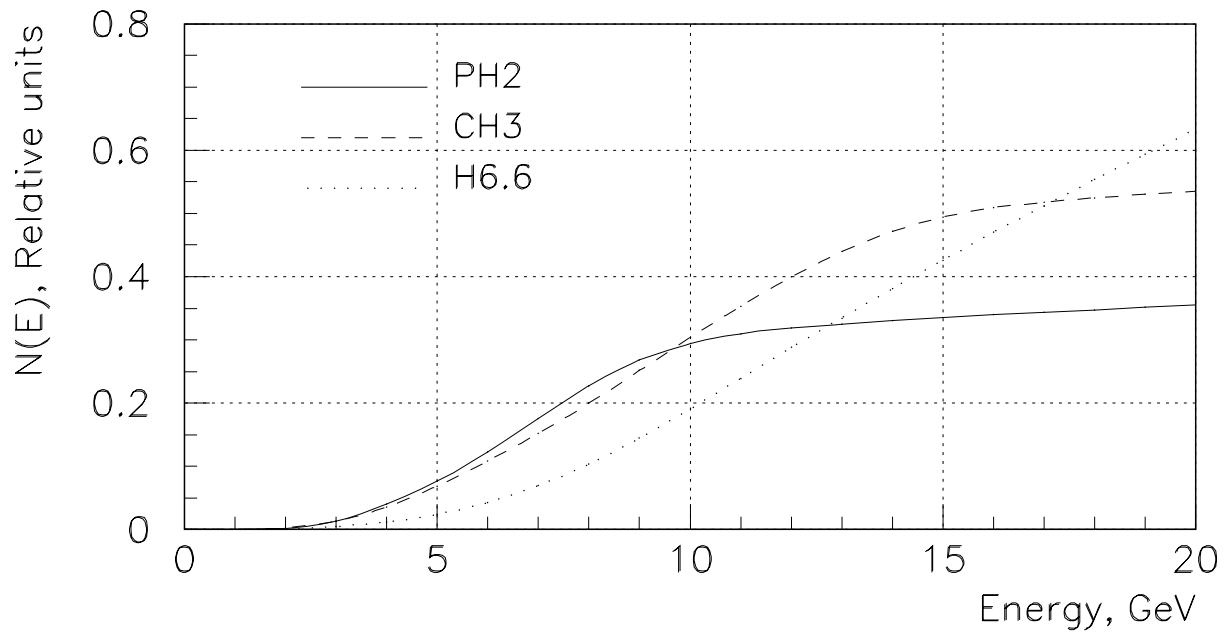


Figure 2.6: The $N(E)$ functions for the PH2, CH3 and H6.6 designs (1.0 corresponds to the H6.6 total ν_μ event rate).

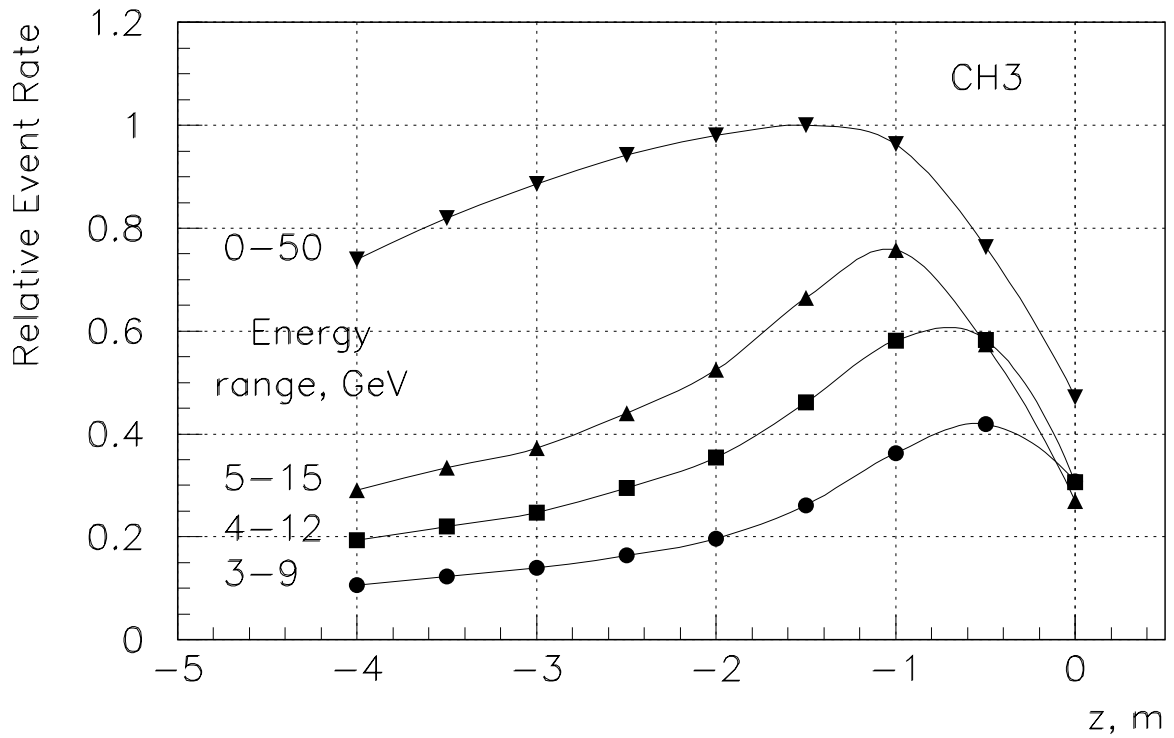
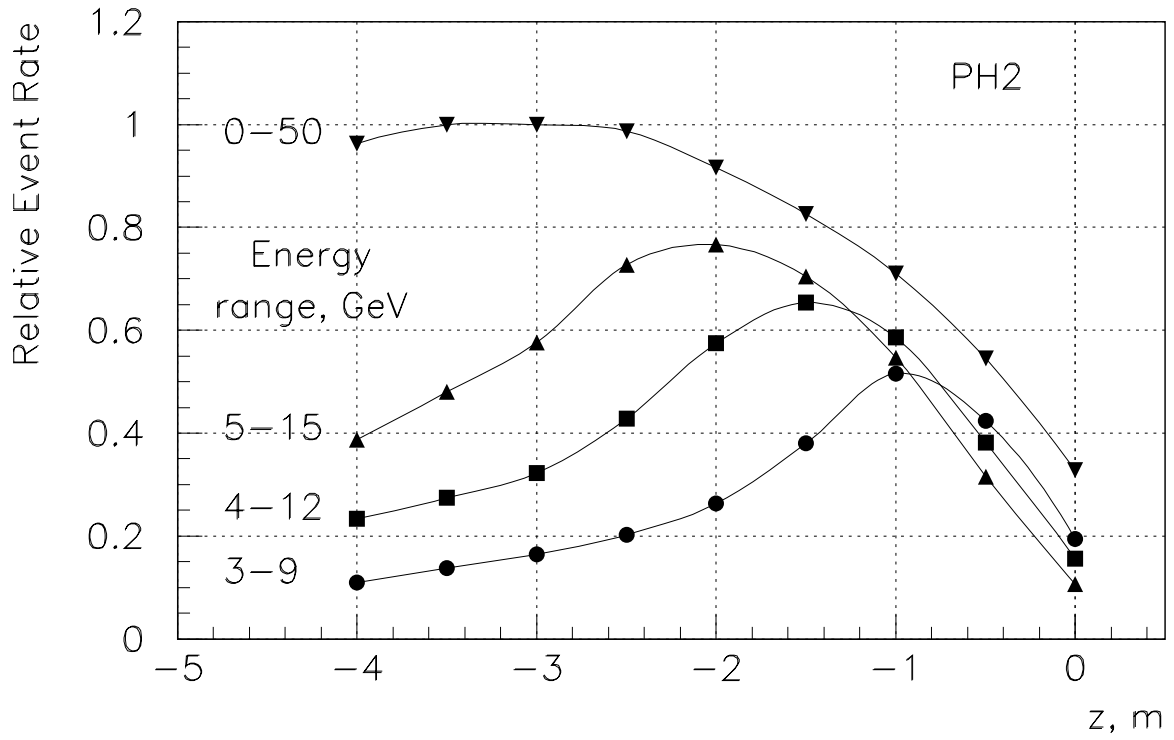


Figure 2.7: Depth of focus in the different neutrino energy ranges for the PH2 and CH3 designs ($z = 0$ is upstream end of Horn#1).

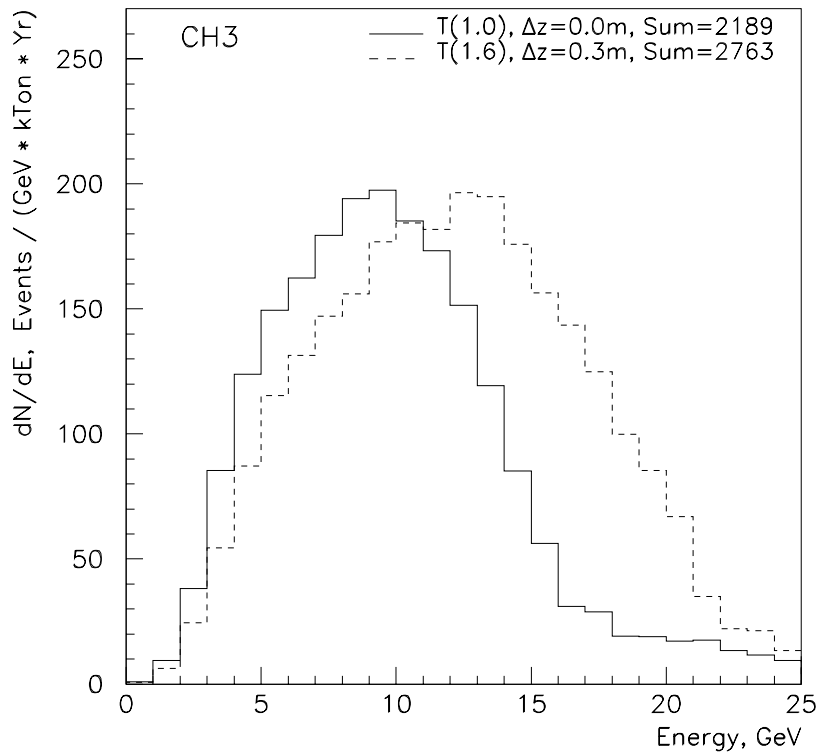
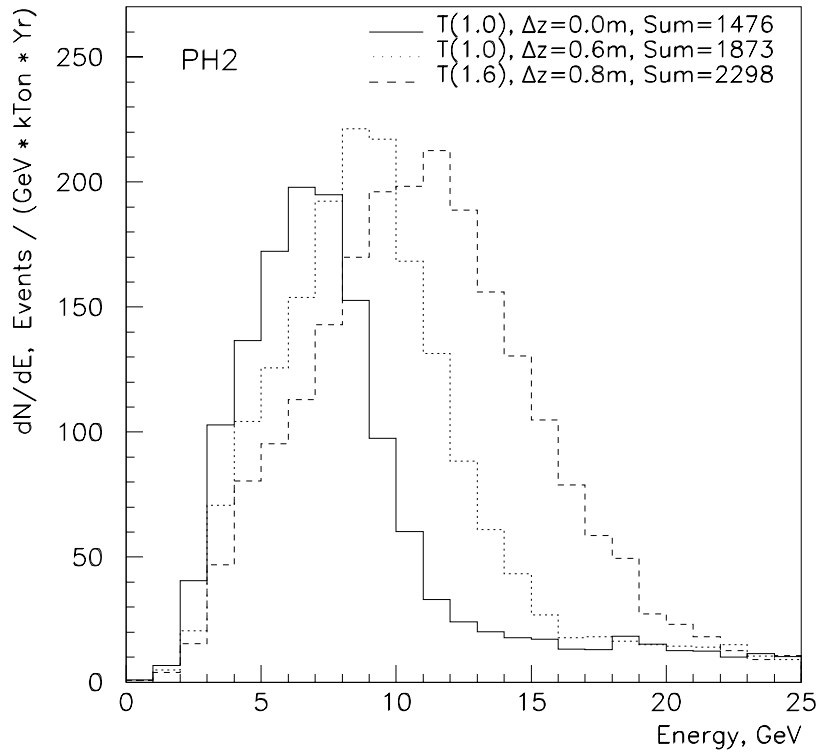


Figure 2.8: The ν_μ charged current event rates for the PH2 and CH3 designs with different targets T(L) (see explanation in text). Δz is the gap between the target and Horn#1.

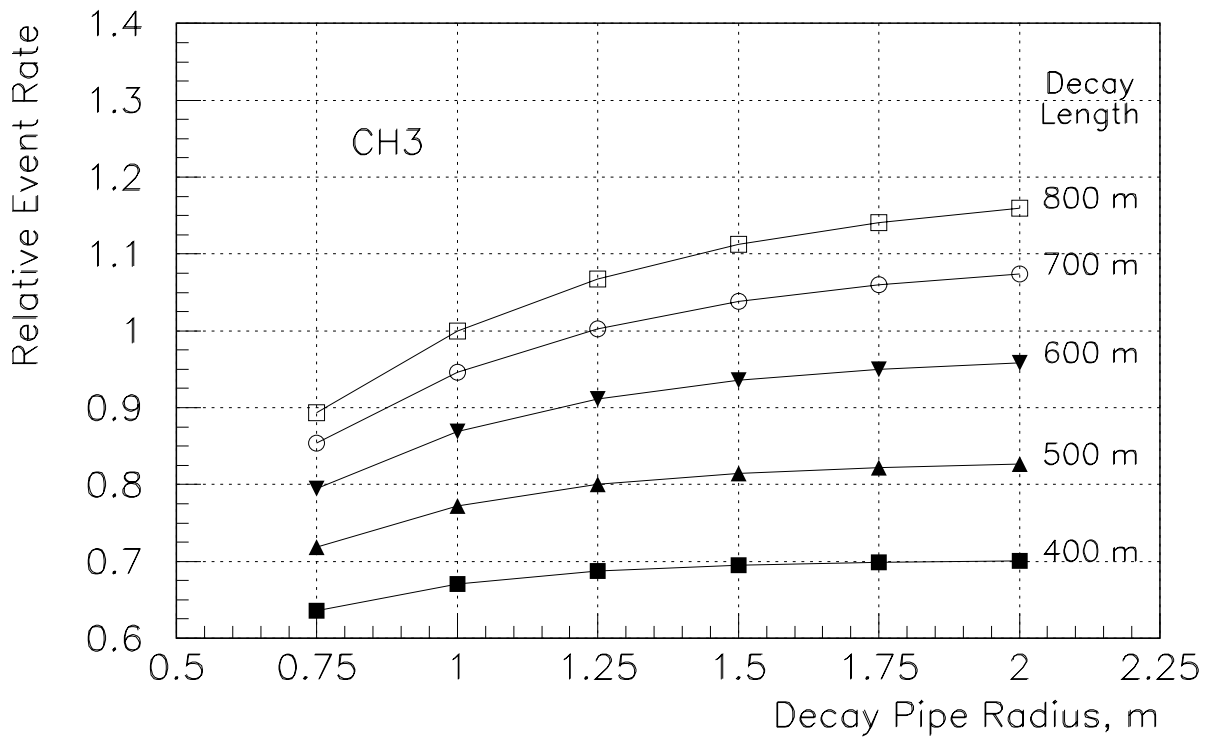
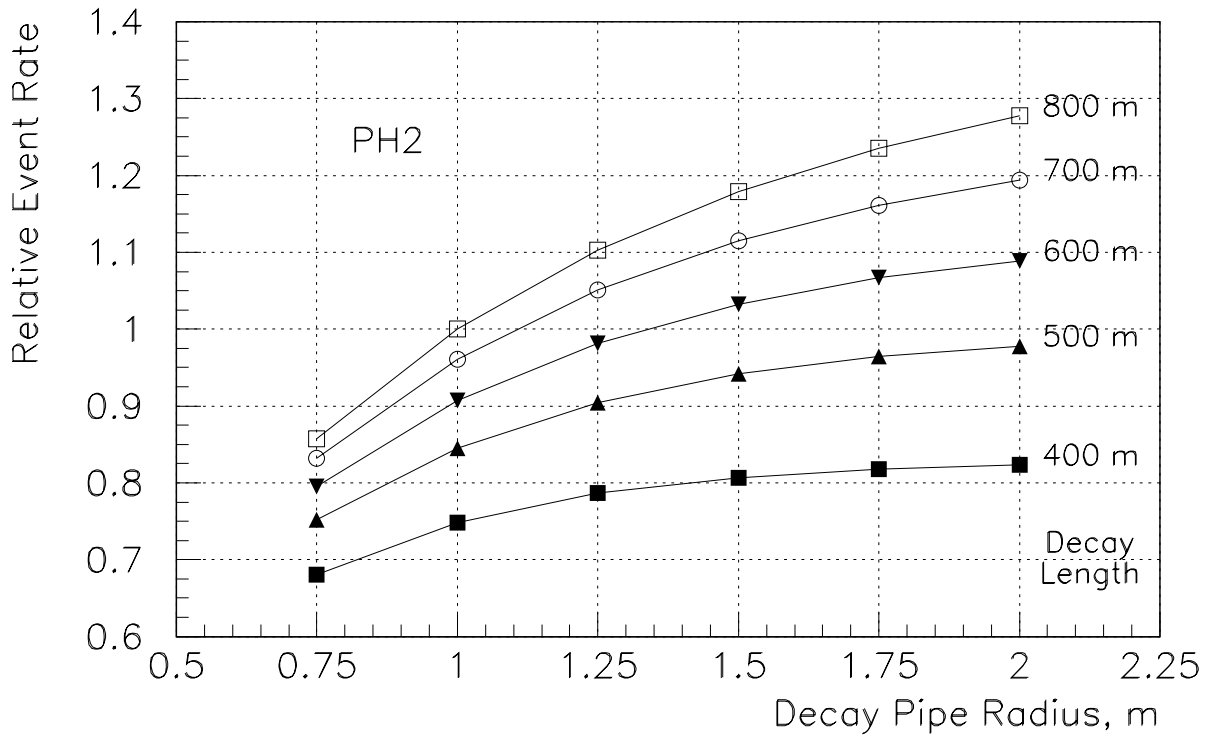


Figure 2.9: Comparison of the ν_μ event rates at the far detector for various decay lengths and decay pipe radii for the PH2 and CH3 designs.

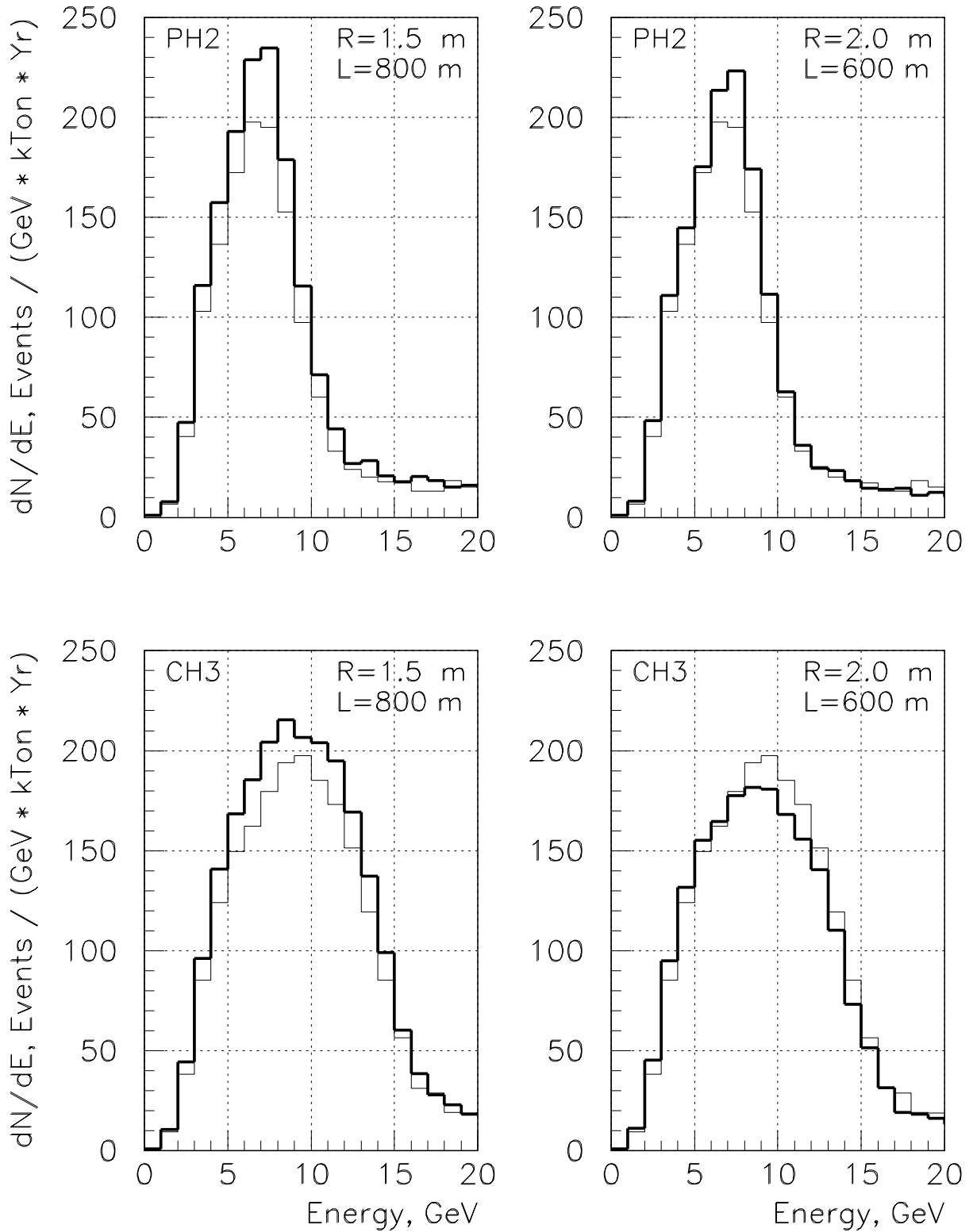


Figure 2.10: The ν_μ charged current event rates for the PH2 and CH3 designs for various decay region lengths L and decay pipe radii R in comparison with spectra for $L = 800$ m and $R = 1.0$ m.

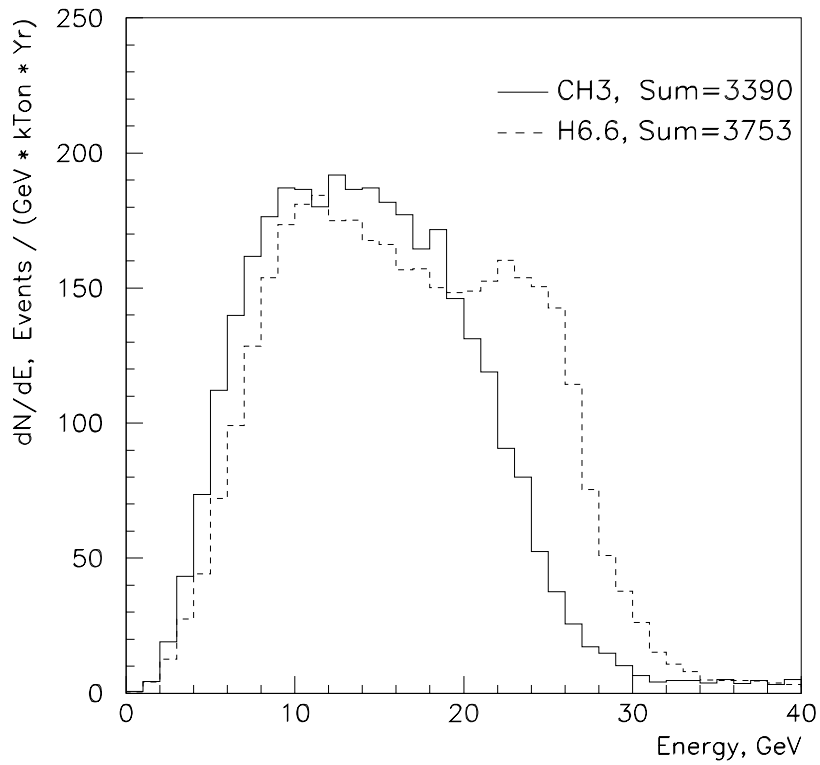
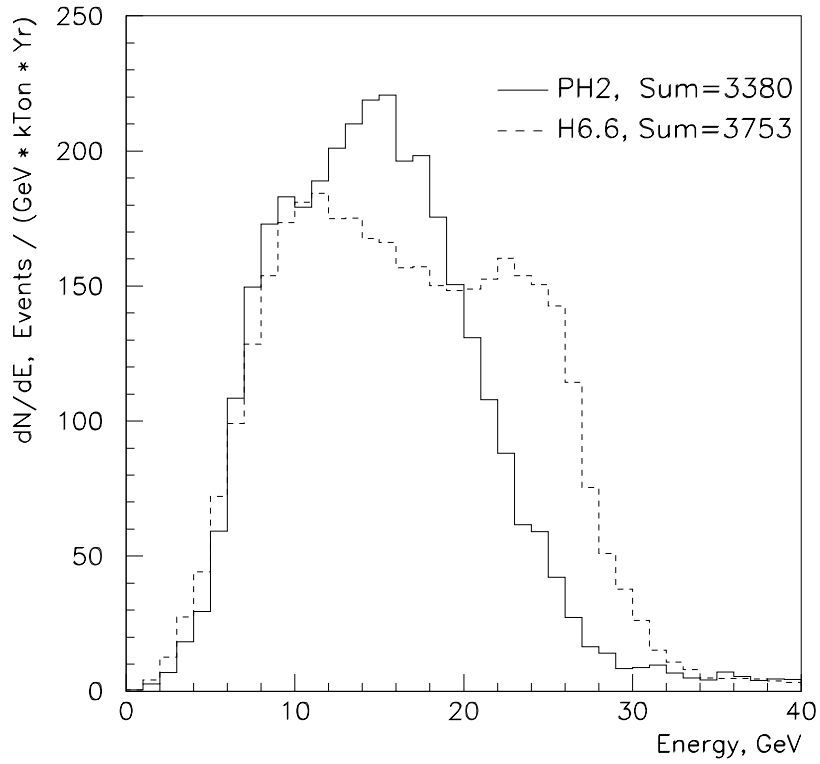


Figure 2.11: The ν_μ charged current event rates for the PH2 and CH3 designs modified to obtain higher energy neutrino beam.

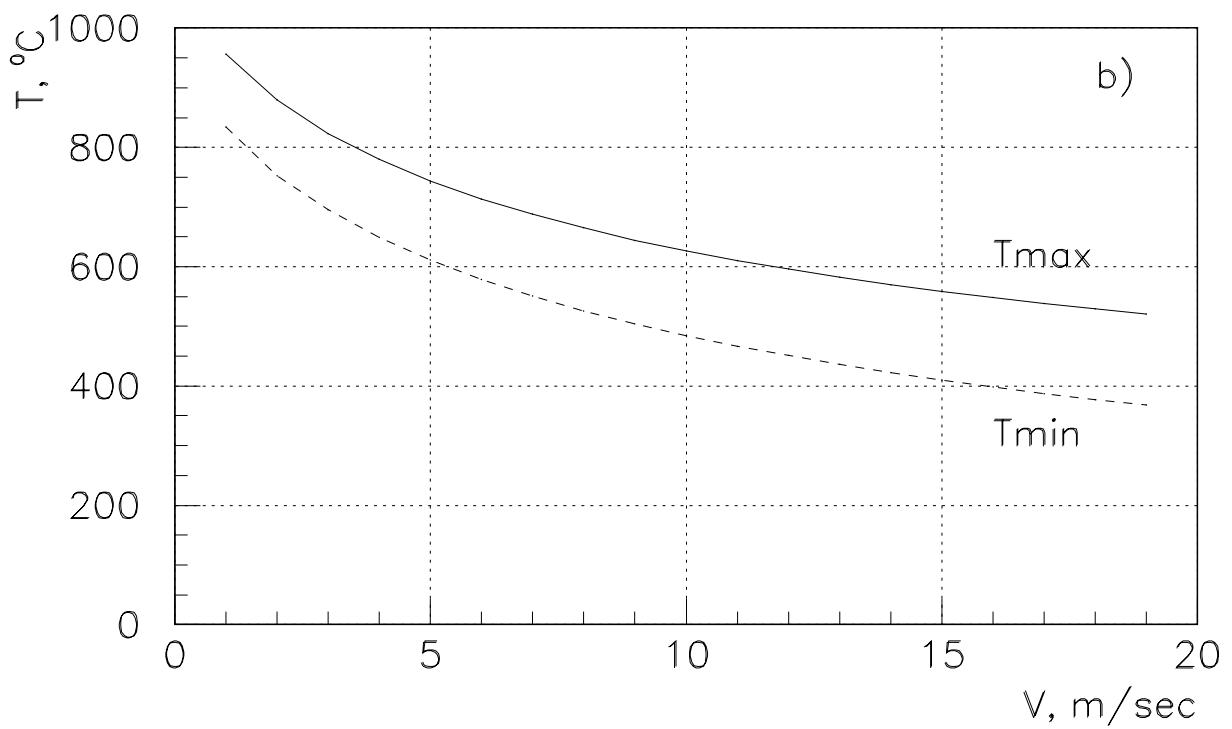
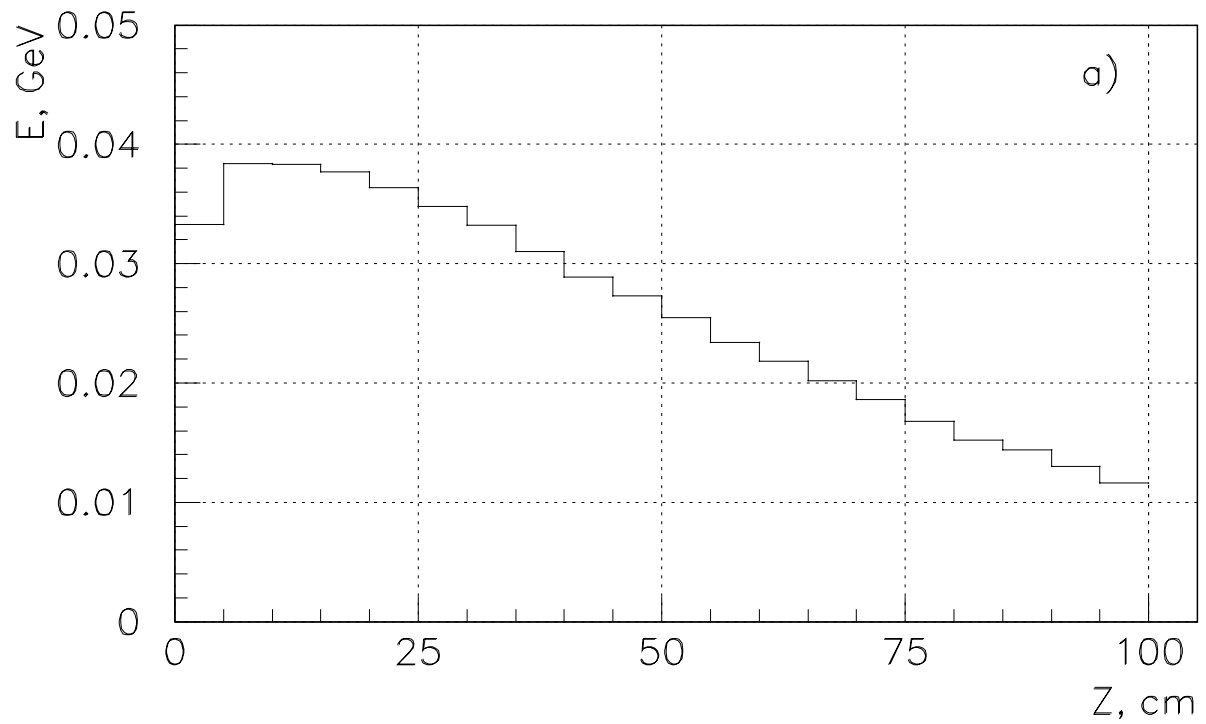


Figure 2.12: The energy deposition distribution per one proton along the target (a); the maximum and minimum temperatures of the most heated part of the target as functions of helium flow velocity (b).

References

- [1] Preliminary Design Work on NBB Absorber and Target Prototype, Protvino, 1998.
- [2] I.Azhgirey et al, Proc. XV Conference on Charged Particles Accelerators, p.74, Protvino, 1996.
- [3] M.Reichanadter, Specification for the Design of the MI-40 Abort Core Box, (Engineering Specification 1451-ES-333047) Fermilab, Batavia, 1996.
- [4] M.Reichanadter, C.M.Bhat, C.Crawford, P.S.Martin, A High Intensity Beam Absorber Corebox for the Fermilab Main Injector Abort System, Fermilab, Batavia, 1996.
- [5] A.Abramov et al, IHEP Preprint 84-64, Serpukhov, 1984.
- [6] A.J.Malensek, FERMILAB-TM-1951, Batavia, 1995
- [7] D.Baratov et al, IHEP Preprint 76-87, Serpukhov, 1987.
- [8] Conceptual Design for the Technical Components of the Neutrino Beam for the Main Injector (NuMI), FNAL-TM-2018, NuMI-B-285, Batavia, 1997.
- [9] Status Report: Technical Design of Neutrino Beams for the Main Injector (NuMI), FNAL-TM-1946, NuMI-B-92, Batavia, 1995.
- [10] N.Mokhov, FERMILAB-TM-628, Batavia, 1995.